North Carolina Agricultural and Technical State University

Aggie Digital Collections and Scholarship

2014

Wear Behavior Characterization For The Screening Of Magnesium-Based Alloys

Paul R. McGhee
North Carolina Agricultural and Technical State University

Follow this and additional works at: https://digital.library.ncat.edu/theses

Wear Behavior Characterization for the Screening of Magnesium-based Alloys

Paul R. McGhee

North Carolina A&T State University

A thesis submitted to the graduate faculty

in partial fulfillment of the requirements for the degree of

MASTER OF SCIENCE

Department: Mechanical Engineering

Major: Mechanical Engineering

Major Professor: Dr. Devdas Pai

Greensboro, North Carolina

2014

The Graduate School
North Carolina Agricultural and Technical State University
This is to certify that the Master's Thesis of

Paul R. McGhee

has met the thesis requirements of
North Carolina Agricultural and Technical State University

Greensboro, North Carolina
2014

Approved by:

Dr. Devdas Pai   Dr. Sergey Yarmolenko
Major Professor and Advisor   Co-Advisor

Dr. Jagannathan Sankar   Dr. Zhigang Xu
Committee Member   Committee Member

Dr. Samuel P. Owusu-Ofori   Dr. Sanjiv Sarin
Department Chair   Dean, The Graduate School

Biographical Sketch

Paul McGhee was born on June 12, 1988 in Concord, North Carolina. He received a Bachelor of Science in Mechanical Engineering from North Carolina A&T State University in December 2011. Paul joined the Master of Science program in Mechanical Engineering at A&T in August of 2012. He worked as a teaching assistant in the Department of Mechanical Engineering during the of 2012-2013school year and a research assistant for the National Science Foundation Engineering Research Center for Revolutionizing Metallic Biomaterials from the summer of 2013 until the completion of his degree requirements. As a graduate student, Paul was a member of the Golden Key International Honors Society and active member of the Student Leadership Council at the Engineering Research Center.

Dedication

I would like to first thank God for providing me strength and guidance on becoming a better person each and every day. This work could not have been completed without God. I would also like to give thanks to my family and friends for their love and support! Especially my wife, Tacara Riley McGhee for letting me completes my research to the best of my ability and for listening to my engineering interest. To my baby girl, Kennidi Riley Smith, thank you for all your support and for taking time out of your little busy schedule to listen to my presentation. Thank you, Jeremiah and Malachi Royster for being patient with me throughout this journey. Again God I thank you again for all that you have done!

Acknowledgements

To Dr. Smith, thank you for taking the time to help me around the lab and around the ERC.

To Nan, Zhao, thank you for taking the time on helping me with SEM microscopy

To my lab mates, thank you for all the good times we had at the ERC.

Table of Contents

List of Figures

List of Tables

Nomenclature and Symbols

Al	Aluminum
BCC	Body-centered cubic
Ca	Calcium
Co-Cr	Cobalt-chromium
CP-Ti	Commercial pure titanium
ELI	Extra low interstitial variant
ER10	Extrusion ratio 10
ER50	Extrusion ratio 50
ERC	Engineering Research Center
FCC	Face-center cubic
Gd	Gadolinium
HCP	Hexagonal close packed
Mg	Magnesium
MZCR	Mg-Zn-Ca-RE alloy
OM	Optical microscopy
RE	Rare earth
SEM	Scanning electron microscopy
Sn	Tin
T4	Solution heat-treatment
Ti	Titanium
V	Vanadium
Y	Yttrium

Zn   Zinc

Zr   Zirconium

Abstract

This research is focused on the development of a systematic approach to evaluate the selection of materials for Mg-based alloys under wear conditions for biomedical applications.

A pilot study was carried out in order to establish an accurate and reliable wear testing technique for magnesium and its alloys. This pilot study was conducted on aluminum (Al) and pure Mg, and showed that aluminum has a lower wear rate compared to Mg. The technique displayed good repeatability and high precision. For the main study, an ERC Mg-based alloy was to be compared with pure Mg. The same technique, when applied to pure Mg from a different vendor, produced up to 90% scatter in the data. Microstructure was studied to see if it had any correlation with the scatter. It was discovered that Mg ingot from the second vendor had outsized grains that contributed to the disproportional scatter in the wear data. Increasing the stroke length during wear testing was required so that the wear data would be averaged over multiple grains and reduces the variation in computed wear rates.

In the main study, wear behavior and friction properties were analyzed using microtribometery, mechanical stylus profilometry, and microindentation. Surface morphology and microstructure were characterized using optical microscopy, scanning electron microscopy, and optical profilometry.

For the main study, pure Mg and the ERC alloy as-cast and extruded conditions were compared. Pure Mg and MZCR alloys were extruded at 350°C and 400°C, respectively. Mg and MZCR alloy were cast at 350°C and heat treated at 510°C. The extruded specimens were divided into two sections, cross-section and longitudinal section. Wear tests were carried out under the applied normal load 0.5 N - 2.5 N in 0.5 N increments sliding at a rate of 0.2 Hz for 240 passes.

The results show that the alloying and extrusion processes increase the hardness of the MZCR

alloy significantly up to 80%. The as-cast MZCR has a lower resistance to wear compared to as-

cast pure Mg. However, the extrusion process enhances the alloy wear resistance as the extrusion

ratio increases. On the other hand, the extrusion process on Mg decreases its wear resistance and

hardness properties. The wear resistance was greater in the cross-section for the pure Mg with

extrusion ratio of 10 and for the MZCR alloy extruded at ratios of 10 and 50. The cross-section

of the MZCR alloys had the lowest amount of wear compared to the longitudinal section.

CHAPTER 1

Introduction

1.1 Background

The mechanics of the human body are similar to those of an automobile which relies on moving components in order to perform its normal operations. Over time, parts and components wear out and need attention in order to function properly. The most common automobile components to experience wear on a regular basis are the brake pads and rotors. Wear occurs due to tribological contact between two opposing surfaces: the brake pads and rotors. Similar to a vehicle, the human body experiences wear daily in the musculoskeletal system that can affect several areas, such as muscles, cartilage, tendons, bones, ligaments and other connective tissues. This ends up limiting the stability and mobility of the musculoskeletal system required in order to carry out daily activities. Also, normal aging of the human body results in some type of wear and tear in the musculoskeletal system due to various forms of physical activities, accidents and diseases. Arthritis of the hand, degenerative disk diseases, and temporomandibular disorders are a few examples of diseases that occur in the body due to bone on bone wear.

According to the National Health Interview Survey [1], about 110 million adults were reported to have musculoskeletal condition in the United States in 2008, with 69% of them being over the age of 75. Debilitating musculoskeletal diseases and disorders have caused people to have limited movement, which have resulted in the loss of days at work. The economic impact of people suffering from musculoskeletal diseases and disorder is estimated to cost about $287 billion annually, which in turn, costs American society about $950 billion yearly [1]. Besides adults, thousands of children younger than 19 years old suffer from musculoskeletal diseases,

These children require assistance with daily activities and about five million suffer from various injuries [2]. Musculoskeletal conditions are a combination of both acute and chronic injuries involving muscles, tendons, ligaments, peripheral nerves, joint structures, bone and associated vascular systems affected by high impact events, degenerative diseases, and infections. Musculoskeletal injuries can be caused by over-exertion in daily activities, automobile accidents, sudden falls, random acts of violence, war, stress, obesity, workplace activities involving repetitive routines, and sports activities [3]. Other causes of musculoskeletal injuries are bone and joint diseases such as osteoporosis, osteoarthritis, rheumatoid arthritis and other inflammatory reactions.

The number of elderly citizens over the age of 65 years is expected to double by 2030. As the population continues to age, the demand for implantable medical devices continues to rise. A study [4] conducted by the Fredonia Group Inc. forecasted that the use of implants in various biomedical applications would increase by 7.7% annually, reaching a value of $52 billion in the year 2015. Of this, the orthopedic implant market alone is expected to reach a value of $29.4 billion in. 2015. Implants are manufactured to provide support or replace a defective body part such as a fractured or diseased bone. Implants used in orthopedic applications, such as joint prostheses and internal fixators, are fabricated from metals such as stainless steel, cobalt chromium, and titanium and its alloys. Devices that are developed to provide solutions to every day needs can also lead to new problems such as the wearing of materials and the premature failures of implants. In 2007, the DePuy Inc. ASR Hip System metal-on-metal (MoM) hip implant was recalled [5]. About 12-13 % of patients with these hip implants had the implants fail within five years after their first surgery. Patients experienced issues such as bone fractures, cobalt-chromium poisoning, metallosis, muscle and nerve damage, dislocation of the hip joint

and implant loosening. In 2008, the Zimmer Durom Cup was recalled due to an ineffective plasma coating that did not promote bone growth. Also, a lack of bone cement caused the socket to float around in the hip joint. In 2013, Stryker Spine had a recall of their OASYS Midline Occiput Plate due to post-operative fracture of the pin that connects the tulip head to the plate spine [6]. Settlements from lawsuits have cost DePuy Inc., Zimmer, and Stryker respectively about $4 billion, 600 million, and $700 million (the last of these could potentially rise to $1.13 billion). These are a few examples of implants that were recalled in the previous years, which lead to the loss of billions of dollars due to liability.

1.2 Problem Statement

Metallic biomaterials have been the popular material of choice in orthopedic applications. Metallic biomaterials make up about 70-80% of the implant materials used in hard tissue support and reconstruction [7]. Metallic orthopedic devices are designed to support the load at the site of injury, allowing the bone to properly heal. The most common metals used in orthopedic devices are stainless steel, cobalt chrome alloy, titanium and its alloys due to their good biocompability, corrosion resistance, and mechanical properties. These classes of metals are used in permanent implant applications to support the healing of bone. The literature [8, 9] reports that various complications that have been associated with using stainless steel, titanium and its alloys, and cobalt-chromium alloys in implants, such as aseptic loosening, migration, breakage, tissue irritation that may initiate localized osteoporosis, resulted from stress-shielding. All these complications can lead to the need for secondary surgery to remove the failing implants.

The complications from these implants have underscored the need for extensive testing procedures to address tribological concerns, and study of a new class of materials: biodegradable materials. The benefits of using biodegradable materials are that they can be designed to have

desirable properties; especially in the area of mechanical and corrosion properties, and should be able to decompose while remaining biocompatible and bone growth in a suitable time frame. Magnesium (Mg) and its alloys have been shown to be promising candidates as a new class of degradable biomaterials [10]. Mg possesses mechanical properties similar to bone, and has good biocompability, reducing the stress shielding effect of the implant-bone interface and minimizing foreign body reactions. Pure Mg does not by itself possess adequate mechanical and corrosion properties for use in orthopedic devices, but through alloying, its properties may be enhanced to meet the requirements of load-bearing applications.

Investigating the tribological properties helps address other issues and concerns with the use of magnesium and its alloys and other biomaterials, in general, as implant devices. Tribology helps provide an understanding of the materials' behavior in design systems that address real world situations, especially when materials are subjected to wear in corrosive environments. Studies can assist in the selection and development of materials that can minimize and control wear and corrosion phenomena. Interest in magnesium alloys continues to rise, but friction and wear behavior data for these alloys are very limited. There are a few studies reported in the literature on the tribological properties of a few magnesium alloys such as AZ91 [11, 12],AZ31 [13], ZE41A [12, 14-16], AZ61 [17], Mg-11Y-5Gd-2Zn alloy [12], and Mg-Zn-Y alloy [12, 15, 18]. Despite the number of tribological studies conducted on these other magnesium alloys, there is limited information on the wear behavior of magnesium alloys containing zinc (Zn), calcium (Ca), and rare earth (RE) simultaneously.

1.3 Objectives

The purpose of this study is to develop an approach for material selection for magnesium-based alloys subjected to wear in biomedical applications by:

I. Establishing necessary techniques for comparative wear evaluation

    a. Establishing testing parameters and necessary equipment that will ensure accuracy and repeatability of data.

    b. Evaluating the effect of microstructure on wear properties.

II. Applying this methodology to evaluate an Mg-Zn-Ca-RE (MZCR) alloy developed by the ERC and comparing with the standard material (pure Mg).

CHAPTER 2

Literature Review

2.1 Biomaterials

Biomaterials are nonviable materials designed to interact with biological systems in order to fulfill or replace some important functions [19-21]. They can be applied to various applications such as biotechnology, tissue engineering, gene transfer, drug delivery, and medical devices. The use of biomaterials dates back to ancient times. According to the literature, around the year 600 B.C., Hindu surgeons repaired an injured human nose by removing living flesh from the patient's cheeks and transferring it to the injury site. This reconstruction technique was later perfected in the West around the 1430 A.D. by the Brancas, a Sicilian layman family. The perfected technique was called the Italian method for repair and reconstruction of the nose. Biomaterials consist of four classes of materials: polymers, ceramics, metals, and composites. The four classes of materials have been used in three generations of biomaterials designed to perform specific function in biological environments in order to repair and enhance the function of the human body. Biomaterials must be able to satisfy several requirements in order to be used in practical biomedical applications. Biomaterials must be designed to have mechanical properties that are suitable for their intended use in various parts of the body. Biomaterials must not trigger foreign body reactions, stress-shielding effects, and must be biocompatible, bioactive and in the case of orthopedic implants, be osteoinductive.

First-generation biomaterials came into existence between the 1960s and 1970s. They are based on property matching between synthetic materials and biological materials. First-generation materials were also designed to be bioinert in order to be biocompatible, i.e., with

minimal immune response and foreign body reaction [22-24]. First-generation biomaterials are industrial materials that are readily available and highly resistant to corrosion.

The development of the second generation of biomaterials was between the 1980s and 2000s. The second generation design was capable of achieving bioinertness just as the first generation of biomaterials. This second generation is composed of two types: bioactive and resorbable. Bioactive materials have the capability to initiate action and reaction within their physiological environment. Bioactive refers to the interaction of the materials with the cells, triggering specific cellular responses and behaviors [23-25]. This ability to enrich the biological response enhances the bonding of tissue to material surface [25]. The second type of second-generation biomaterials is resorbable biomaterials. Resorbable biomaterials are designed with a degradation functionality which allows the biomaterial to degrade over a period time. The degradation function would gradually eliminate the interface between the implant site and host tissue [24] as the materials decompose into non-toxic substances soluble in the host's biological system.

The development of the third generation of biomaterials was inspired by the second-generation biomaterials; bioactive and resorbable. The third generation biomaterials combined the concept of bioactive and resorbable into one material, generating bioactive materials that are resorbable and resorbable materials that are bioactive. The aim of the third generation biomaterials is to stimulate specific cellular response on the molecular level [24, 25] for the purpose of provoking and supporting tissue regeneration [23].

In general, the use of biomaterials for an application depends on the type of properties required and the cellular response activated at the material's interface. In the literature, the interfacial bonding between bone and biomaterials is influenced by the level of reactivity of the

biomaterial. The low reactivity of the inert biomaterial leads to poor interfacial bonding with tissues. This poor bonding has been documented to cause relative movement of tissue and implant, which could lead to deterioration in function in both materials [26].

2.1.1 Polymers

Polymers can be categorized by their ability to form under heat and pressure. The three main types of polymers are thermoset, thermoplastic, and elastomer. Thermosetting polymers have the ability to be reformed under numerous heating and cooling cycles without degradation of the polymer properties. During initial heating, thermoplastic polymers undergo a chemical reaction that hardens the materials permanently. Thermoset polymers, unlike thermoplastics, will degrade if subjected to reheating. Elastomers, also known as rubbers, are polymers that have extreme elastic properties and molecular structures similar to thermoplastics.

Polymers can also be classified according to their sequence of monomers and their molecular structure. The two types of polymer based on monomer sequence are homopolymer and copolymer. Homopolymer contain a single type of mer, while copolymers consist of two or more types of mer. The sequence of the copolymer may vary. Depending on the reaction condition and reactivity of the monomer type, this results in random, alternating, block, and graft copolymers. Random copolymers are polymers with random-ordered mers. Alternating copolymers consist of mer repeats in alternating positions. Block copolymers consist of a repeating pattern of groups of different types of mers. Graft copolymers are a chain of a single type of mer acting as the backbone of the polymer connected by another type of mer acting as branches. Polymers can also be synthesized with three types of mers forming terpolymers. Figure 1 shows the possible arrangement of various monomer sequences.
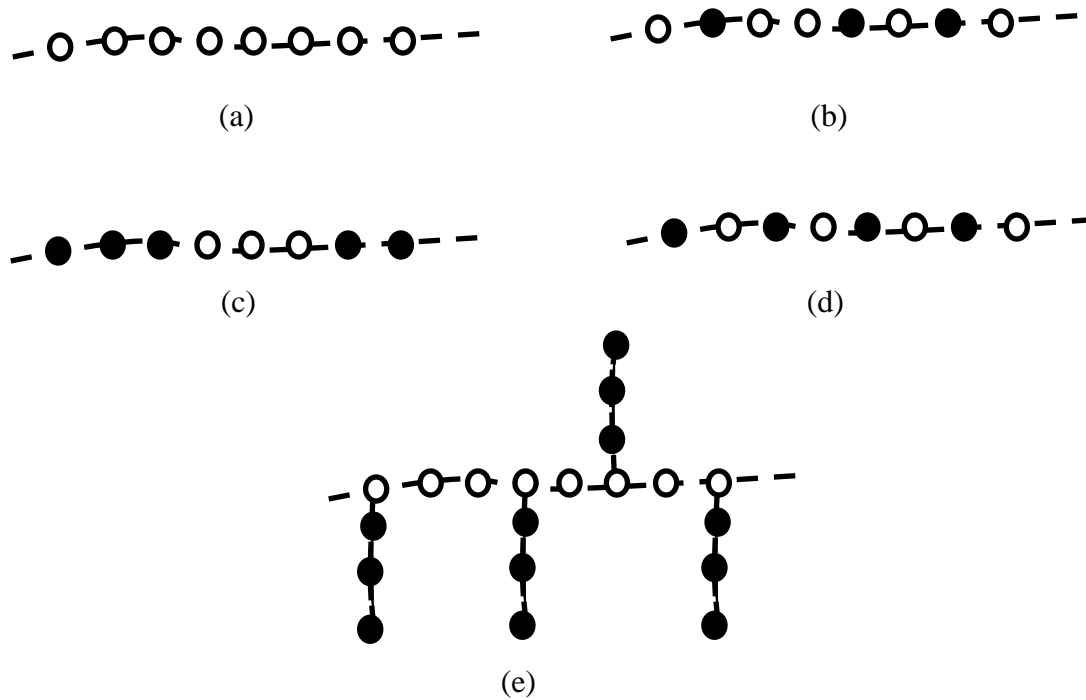
Figure 1. Molecular structure of polymers (a) homopolymer, (b) random copolymer, (c) block copolymer, (d) alternating copolymer, (e) graft copolymer

Polymers may be amorphous, crystalline, or semi-crystalline. Amorphous polymers have a very low to non-existent degree of crystallinity. Crystallinity is defined as the proportion of crystallized material in the overall mass. Amorphous polymers are transparent like glass and could have elastic properties similar to rubber. Crystalline polymers have a high degree of crystallinity. This increases their mechanical properties, such as density, strength, stiffness, toughness, gas permeability, and heat resistance, compared to amorphous polymers. The crystalline polymer cannot attain a fully crystalline structure similar to that of many ceramics and metals. A semi-crystalline polymer is a two-phase system that has a combination of amorphous and crystalline regions within its assembly. The amorphous regions are misaligned chains that are loose, twisted, kinked or coiled. The crystalline regions contain crystallites, a regular arrangement of mers.

Synthetic polymers are synthesized through two growth processes: addition and condensation polymerization [27]. Polymerization deals with the chemical arrangement of monomers and molecules within the molecular structure of the polymer. The process conditions during polymerization can result in various polymer structures such as chain-like structures called linear polymers, linear polymers with branch extension known as branched polymers, branch-to-branch connected polymers called cross-linked polymers, and tightly cross-linked polymers also known as network structure.

Addition polymerization reactions involve unsaturated monomers undergoing chemical reaction in three phases: initiation, propagation, and termination. During the initiation phase, an initiator in the form of radicals, cations, anions, or stereospecific catalysts, creates an initiation site within the monomers by opening the carbon-carbon double bond. During the next phase, propagation, rapid chain growth occurs. When the rapid chain growth reacts with other radicals, polymers, initiators, solvent molecule, or added chain transfer agent, the growth process enters the termination phase, deactivating the polymerization process.

Condensation polymerization is the reaction of two monomers to form a covalent bond, eliminating small molecules such as water, hydrochloric acid, methanol, or carbon dioxide [27]. The monomer units impact molecular weight of the final product, and the distribution of the molecular weight of the condensation-reaction product copolymer.

Biopolymers are the largest class of materials used in biomedical applications that include orthopedics, dental, hard and soft tissue replacement and cardiovascular devices [23]. Polymers have been used throughout the history of medicine. Reports of the uses of polymeric biomaterial date back to the 1940s. Poly-methyl-methacrylate (PMMA), poly-acrylamide (PA), poly-acrylic-acid (PAA), high-density polyethylene (PE), poly-vinyl-chloride (PVC),

polypropylene (PP), polydimethylsiloxane (PDMS), poly-ethylene terephthalate (PET), cellulose acetate (CA), polyglycolic acid (PGA), poly-L-lactic acid (PLLA), poly-DL-lactic acid (PDLLA), PGA/trimethylenecarbonate copolymers (PGA/TMC), poly-p-dioxanone (PDS) and poly-beta-hydroxybutyric acid (PBHBA) are common polymeric biomaterials used in the medical fields [23, 25, 28].

2.1.2   Ceramics

Ceramic materials are inorganic non-metallic solids with a tightly-packed structure, bonded together by various combinations of ionic or covalent bonding [27, 29]. Based on their microstructure, ceramics can be divided into two subclasses: glass-ceramics and glass. Ceramics have three types of crystalline structure: simple cubic (SC), face-centered cubic (FCC), and hexagonal close-packed (HCP) [27, 30]. Glass-ceramics have a mixed microstructure of polycrystalline and amorphous phases. The phases in the glass-ceramics are created by controlled nucleation and crystallization of a base glass. The microstructure contains grains separated by boundaries made of a glass phase and gas-filled pores [29]. The second subclass of ceramics is glasses. Glasses have an amorphous structure (non-crystalline) that is disordered atomically, that is similar to the characteristic of liquid, and a high viscosity that causes it to acts like solids respectively. Ceramics have high hardness, thermal and electrical resistivity, resistance to corrosion and thermal degradation, brittle and fracture behavior without deformation [29].

Ceramics have been used in the medical industry for various applications including eyeglasses, diagnostic instruments, chemical glass, thermometers, tissue culture flasks, fiber optical endoscopy, restorative materials for dentistry, hard tissue repair, and transport for bone cells, growth factors and drugs for bacterial and cancer-related illness. Insoluble porous glasses

have been used as delivery systems for antibodies, enzymes, and antigens. These glasses provide enhanced microbial resistance, change in pH levels, solvent conditions, temperature, and packing under pressure required for rapid flow [26, 27, 29, 31, 32]. Bioceramics have been used for the hard tissue repair of bones, joints, and teeth. Common bioceramics used in orthopedic surgery, traumatology, and dentistry are hydroxyapatite (HA), calcium phosphate, tricalcium phosphate (TCP), alumina, zirconia, titania, calcium aluminates, bioglass, apatite-wollastonite (A-W) glass-ceramics, plasma-sprayed HA coatings, and calcium phosphate bone cements [26, 30-32].

2.1.3   Metals

Metals are inorganic materials composed of a combination of metallic and nonmetallic elements in a crystalline structure held together by metallic bonding. The atomic arrangements of metallic crystalline structure are most commonly of the three types: body-centered cubic (BCC), face-centered cubic (FCC), and hexagonal close-packed (HCP). The crystalline structure and bonding characteristics influence the mechanical, thermal, and electrical properties [33]. The properties of metals, such as high tensile strength, fracture toughness, stiffness, fatigue resistance and corrosion resistance, have made metals suitable candidates for load-bearing applications in the medical field [34].

Metallic materials have been used in various medical devices for applications such as orthopedic, dental, and cardiovascular. In orthopedics, metals have been used since the 1920s as implant materials to aid in the replacement or repair of diseased or damaged hard tissue [35]. Metallic implants and devices in the orthopedic surgery have been used for reconstructive joint replacements, spinal, orthobiologics (substances used to accelerate the healing of injuries) and trauma implants [19]. Implants and devices have been fabricated in the form of fixation plates, wires, screws, pins, and artificial joints. Dental devices are designed in the form of partial-

denture framework, porcelain-metal restorations, crown bridges, orthodontic wires, brackets, braces, and implants [32]. Metals have been used in vascular stents, parts for artificial heart valves and defibrillators, balloon catheters, aneurysm clips, and as leads for electrical support of pacemakers in the cardiovascular field. Stainless steels, Ti and its alloys, and Co-Cr alloys have been the choice of metals approved for use in the biomedical field as permanent implants [9, 25, 29, 32, 36-41]. Most recently, magnesium and it alloys have been attracting interest as potential candidates as biodegradable materials for temporary implant applications [9, 10, 38-51].

2.1.3.1   *Stainless Steel*

Stainless steel, along and cobalt-chrome-based alloys were the first metals used in orthopedic applications in the early twentieth century [25]. Stainless steel has a high resistance to corrosion due to its high chromium content (> 12% Cr), which aids in the formation of a Cr_2O_3 thin film layer that is adherent, self-healing, and resistant to corrosion [25] . The majority of pins, wires, screws, plates, intramedullary nails and rods used for internal fixation devices are made of stainless steel, especially of type 316L (also known as austenitic steel), due to their low cost, high availability, and ease of fabrication. Stainless steel alloys are mainly composed of nickel, chromium, and molybdenum, with minor amounts of nitrogen, manganese, phosphorus, silicon, and sulfur [25, 33, 52]. The stainless steel used for implant applications has been standardized in the materials specifications of the ISO and ASTM. These standards provide the specifications for stainless steels composition, microstructure, and the mechanical properties required for internal fixation [53]. Stainless steel is highly ductile compared to the titanium. This ensures the ease of alteration of material geometry without alteration of its mechanical properties. The issue in using stainless steel for internal fixation devices, however, is the excessive stress shielding effect on bone caused by its high elastic modulus. The high rigidity of

a stainless steel implant can affect secondary fracture healing by delaying the formation of callus tissue [36, 54]. Austenitic, martensitic, ferritic, and precipitation-hardened stainless steels for implant and surgical devices are specified in the ASTM standards [32, 37].

Austenitic stainless steels are nonmagnetic materials that can undergo plastic deformation without damage, due to their level of nickel content. They have moderate strength, high ductility (compared to the other steel alloys) and good corrosion resistance for short-term use. This type of steel has been used in non-implantable medical devices such as dental impression trays, guide pins, hollowware, hypodermic needles, steam sterilizers, storage cabinets, surgical work surfaces, and thoracic retractors. Implant devices of austenitic steel are also used as wires, bone screws, plates, intramedullary nails and rods and other temporary fixation devices. Martensitic stainless steels are ferromagnetic materials with a BCC crystalline structure wuth fair corrosion resistance (depending on the pH level) and very high hardness. Martensitic stainless steels have been used to fabricate surgical and dental instruments such as scalpels, orthodontic pliers, chisels, gouges, and curettes, etc. Ferritic stainless steels have been machined for use in handles for instruments, guide pins and fasteners [32].

2.1.3.2   *Titanium and Ti Alloys*

Ti and its alloys are first-generation biomaterials that have been used in orthopedic applications since their introduction in the 1940s [25, 55] due to their mechanical properties such as, low density, high corrosion resistance and high biocompability [33]. Ti and its alloys are highly resistant to corrosion due to the surface formation of a titanium oxide layer which contributes to their biocompatibility and bioactivity. This type of material has the capability to integrate into bone The osseointegrative bioactivity is not sufficient enough to attain true adhesion between the implant and bone [19]. This insufficiency of osseointegrative bioactivity

can lead to mechanical instability and failure of implant devices. Titanium has been used in biomedical applications, such as bone screws, plates.. Ti has low wear resistance when making tribological contact with itself and other metals. Ti alloys under wear tend to have a high coefficient of friction, which leads to the production of wear debris. The wear debris generated can activate foreign body reaction, which can cause inflammatory response of the surrounding tissue. This can result in implant stability due to osteolysis [56].

Commercially pure titanium (CP-Ti) and an extra-low interstitial variant of titanium alloy Ti-6Al-4V called Ti64-ELI are used in biomedical applications, among other titanium alloys [27, 56-60]. Compared to stainless steel, the resistance to corrosion is higher in CP-Ti, and tissue inflammatory reaction is minimal. Applications of CP-Ti are limited due to its lower mechanical strength and poor wear resistance. CP-Ti strength can be enhanced through cold working processing. CP-Ti has been used in pacemaker cases and heart valve cages, cardiovascular stents, lead wires, fixation , reconstruction devices, and dental and maxillofacial application [55, 59]. The properties of Ti64-ELI such as high strength, and low elastic modulus, excellent corrosion resistance and good tissue tolerance caused a heighten interest in them in the USA towards the late 1970s. Ti64-ELI has gained attention for medical applications. Ti alloys have been fabricated into hip and knee prostheses, internal fixation devices, dental implants, and other medical instruments [55]. Newer titanium alloys have been introduced for implant applications identical to those served by Ti64-ELI due to the implant device reliability and health concerns related to Ti-ELI. According to the literature [7, 36, 55, 56, 61-63], vanadium has been proven to cause cytotoxic effects in biological environments and aluminum has been linked with long-term health problems such as Alzheimer's disease, neuropathy and ostemomalacia. To address these

concerns, research has been focused on the development of vanadium and aluminum-free Ti alloys such as Ti-Zr-, and Ti-Sn-based alloys.

2.1.3.3   *Cobalt-Chromium Alloys*

Cobalt-chromium (Co-Cr) alloys contain cobalt and chromium mixed with other elements, such as molybdenum and nickel, to enhance their mechanical properties. The mechanical properties of Co-Cr alloys are marginally higher than those of stainless steels. Their elastic modulus (220-230 GPa) is within range of the ~ 200 GPa elastic modulus of stainless steel. However, compared to the 20-30 GPa elastic modulus of the human bone, Co-Cr alloy is an order of magnitude stiffer and as an implant device, the majority of the load would be transferred to the device. As the implant absorbs the load, a stress-shielding effect is produced in the bone, causing resorption of bone tissue which can lead to implant instability. Another drawback of using Co-Cr alloys beside stress-shielding effect is poor osseointegration, high cost, poor fabrication [19, 25, 36].

Compared to stainless steel and Ti alloys, Co-Cr alloys possess higher wear resistance and high strength properties. This makes them suitable for the femoral head in hip prosthesis [7, 37, 52]. Co-Cr alloys have found used in other biomedical applications such as knee and hip replacements, tibial trays, acetabular cups, dental components, pacemakers lead casing, and cardiovascular stents.

2.1.3.4   *Magnesium and Mg Alloys*

Mg and its alloys have become the research focus as candidates for biodegradable implant applications [42]. Mg was first discovered in 1808 by a British chemist, Sir Humphrey Davy. The earliest clinical use of magnesium as a biodegradable implant was in 1878 by physician Edward C. Huse. Dr. Huse used Mg wire as ligatures to close bleeding in the radial

artery and varicocele. Beside ligatures in cardio applications, magnesium has been used in mesh wires (Gotthard Gossrau, 1935), hemostatic clips (Richard Jorgensen, 1986), vessel connectors (Erwin Payr, 1900). In 1900, Payr introduced the use of magnesium in the forms of plates, sheets, screws, pins, nails wires, pegs, clamps for musculoskeletal applications [64].

Mg and its alloys are exceptionally light-weight metals with densities between 1.74 - 2.0 g/cm^3 and elastic modulus ranging from 41 - 45 GPa. These numbers are close to those for human bone materials (1.8 - 2.1 g/cm^3, 3 - 20 GPa) [9, 38-40, 45, 48] as compared to traditional non-degradable implant materials like stainless steel, Co-Cr alloys and Ti alloys (see Table 1).

Table 1. Comparison of biomaterials with natural bone*

Properties	Natural bone	Mg	Ti alloy	Co-Cr alloy	Stainless steel
Density (g/cm^3)	1.8-2.1	1.74-2.0	4.4-4.5	8.3-9.2	7.9-8.1
Elastic Modulus (GPa)	3-20	41-45	110-117	230	189-205
Compresive. Yield Strength (MPa)	130-180	65-100	758-1117	450-1000	170-310
Fracture Toughness (MPa·m$^{1/2}$)	3-6	15-40	55-115	N/A	50-200

*Compiled from references [9, 38, 40, 45, 48, 52]

The corrosion products of Mg are non-toxic. Mg is an alkaline earth metal that is beneficial to the human body it is the fourth most abundant cation in the body. It is found stored in bone tissue, and promotes bone growth [9, 46, 48]. Mg is a cofactor for many enzymes and stabilizes the structure of DNA and RNA [9, 48, 49]. Low corrosion and wear resistance are major setbacks for pure Mg, since this can affect the mechanical integrity of the implant materials [12, 15, 49, 65]. The corrosion behavior and the mechanical properties of magnesium

can be improved through alloying and protective coating techniques while ensuring that material remains biocompatible [9, 46, 65]. Modification of the material's surface and composition to retard the corrosion rate is desirable, so as to allow sufficient time for the healing tissue to gain strength as the implant gradually degrades, and loses its ability to support. This controlled biodegradability is what would eliminate the need for secondary surgery.

The properties of magnesium can engineered to meet the requirements of implant designs by alloying with different elements to tune the various properties required for particular implant applications. Enhancement of the magnesium mechanical properties can be achieved through precipitation hardening and / or solid-solution hardening [66]. The manufacturing processing for magnesium alloys can be found in the ASTM Standard. The alloying elements that have been used for magnesium are aluminum (Al), zinc (Z), calcium (Ca), and rare earths (RE). Al has been used raise the tensile properties via formation of an intermetallic phase [66]. Ca has been found to be an important constituent element in human bones. By adjusting the amount of Ca in the alloy, desirable mechanical properties can be obtained. The drawback of Ca in Mg is that the resulting mechanical properties and corrosion resistance are not sufficient for biological applications. Similar to Ca, Zn is very important to the human body and can improve the mechanical and corrosion properties of Mg [46].

2.1.4   Composites

Composite materials are a combination of two or more phases bonded together so that the transference of stress occurs across the phase boundary [29]. Composites can be fabricated to achieve desirable material characteristics and properties by extracting the best characteristics and properties from the constituent materials. Composite materials can be classified based on their matrix or reinforcement dimensions and shapes, such as particulates, short fibers, and continuous

fibers [67]. There are three types of composite based on the type of matrix material: polymer-, metal-, and ceramic-matrix. Composite materials can be categorized according to their bioactivity levels as: bioinert, bioactive, and bioresorbable. Composites can also be classified by the type of reinforcement. There are two types of reinforcement: fibrous and particulates. Fibrous biocomposite contain of numerous fibers within the composite matrix. Laminates are a special type of composite made multiple stacked fiber composite laminae [33]. The second type of composite based on reinforcement is the particulate composite. Particulate composites are isotropic materials with increased toughness in all directions, sacrificing the level of flexibility and stiffness. Porous composites are a special type of particulate composite where the inclusion phases are hard. They have found use in soft- and hard-tissue repair and replacement by promoting tissue ingrowth [33].Biocomposite properties are strongly influenced by several factors such as reinforcement geometry and size distribution, reinforcement and matrix properties, reinforcement volume fraction, bioactivity of the reinforcement and matrix, distribution of reinforcement in the matrix and reinforcement-matrix interfacial state [67].

2.2 Tribology

Tribology is the science and technology of friction, lubrication and wear [68] of materials. The Greek word *tribos-* is means as rubbing [69, 70], thus tribology studies the interaction between contacting surfaces in relative motion. Tribological contact can generate changes in the material's physical, mechanical, and/or chemical properties. The word tribology was first introduced in the 1966 Jost Report to the United Kingdom Department of Education Science by Professor H. Peter Jost [69, 71]. The report concluded that the department depleted millions of pounds due to ignorance of friction, wear, and corrosion. According to [71], about 6% of the US gross national product (GNP), which amounted to 900 billion dollars per year due

to the lack of importance given to tribological research. Tribological research requires multi-disciplinary knowledge since the studies of surface interactions at tribological interface are highly complex [69]. Tribological studies can provide potential solutions to industries, ranging from automotive to medicine, which could tremendously help improve society economically and ecologically.

Tribological research is aimed towards the optimization of friction and wear in various applications to achieve high efficiency and sufficient reliability while reducing maintenance and manufacturing costs. Information about the tribological environment and the material's physical, mechanical and chemical behavior can be used to improve product design to make the product more suitable for its intended application. Tribology can save resources, money, and improve technology.

Tribological phenomena occur daily inside the human body, e.g. the rubbing of cartilage-on-bone and bone-on-bone. The understanding of tribological phenomena plays a key role in the development of reliable dental and orthopedic implant applications. In dental applications, the chewing process involves rubbing contact between food particles and the tooth in a wet environment composed of saliva. The human musculoskeletal system experiences wear tears in tendons, ligaments, and joints due to intense physical activities and, repetitive work routines, unexpected trauma, and bone-related diseases. Orthopedic design implants (such as hip and knee prostheses) are designed to replace or repair a bodily function inside the human body. Implants experience wear due to corrosive environmental interactions that could cause implant materials to degrade. The material-material and material-bone surface interactions influence the rate of wear. Stress-induced corrosion can lead to premature failure.

Tribological phenomena can affect the body's performance as well as the performance of implants. This can potentially cause problems for the patients. Metallic ions are generated from implanted materials by two main factors: corrosion and wear. Corrosion and wear can be triggered by factors such as friction, lubrication, surface morphology, surface chemistry, temperature, and pH level. Corrosion and wear result in the chemical and mechanical removal of materials, respectively. Corrosion and wear products can cause an inflammatory response in the local surrounding tissue, leading potentially to an immunological response (also known as foreign body response). This immunological response can cause blood clotting, release of leukocytes and macrophages would intercept the corrosion/wear particles that can lead to issues between implant and bone. By understanding the tribological behavior of body joints, organs, and teeth, would allow biomedical devices to be modified in order to increase the device life span. This would decrease the patients' need for revision surgery, allowing them to enjoy the positive benefits of their implant devices and also saving billions of dollars [72].

2.3 Wear

Wear is the process of material removal from one or both of the surfaces in tribological contact. During this phenomenon, the softer surface undergoes plastic deformation, causes damage to the articulating surface and generates wear particles. As mentioned earlier, the human body is composed of several moving components in tribological contact that must coordinate with each other for stability as well as motion. Similar to man-made devices, through natural processes and frequent use, various parts of the body are adversely affected by tribological phenomena, jeopardizing long term performance. Wear-related disorders such as osteoarthritis, degenerative disk disease, and temporomandibular disorder involve the rubbing of bones. This

induces wear that can change the properties of bone, potentially leading to chronic pain that may require medical attention.

Wear is one of the leading causes of implant failures due to the newly-spawned wear debris that can initiate inflammatory response. Wear has been reported to cause failure in biomedical devices such as hip and knee prostheses and even fatality in extreme cases, such as mechanical heart valves [73, 74]. Wear can also change the geometry of the implant device, directly affecting and diminishing the device function capability, reliability, and work life.

Wear phenomena can occur through various wear mechanisms such as abrasion, adhesion, delamination, fatigue, fretting, and corrosion. Wear is not a material property but a system response [75]. Wear properties describe the response of a pair of materials in contact in a tribosystem. The process of wear starts at highly stressed points of localized contact that experience fracturing, shearing, or flow. That results in the production of wears debris. Wear can be influenced by several factors such as temperature, surface roughness of contacting materials, the speed of relative motion, contact geometry, and environment conditions.

2.3.1   Contact Mechanics

Sliding wear between solid surfaces is based on contact mechanics principles. Solid surfaces have a morphology that contains numerous peaks, known as asperities, on the microscale, as shown in Figure 2. The sliding process can undergo three stages of contact as shown in Figure 3. During static contact, the harder asperities deform the soft asperities and penetrate the surface. The tangential force at this stage is not large enough to transfer the load to the leading side of the asperity that would generate the shoveling of loose material [76].
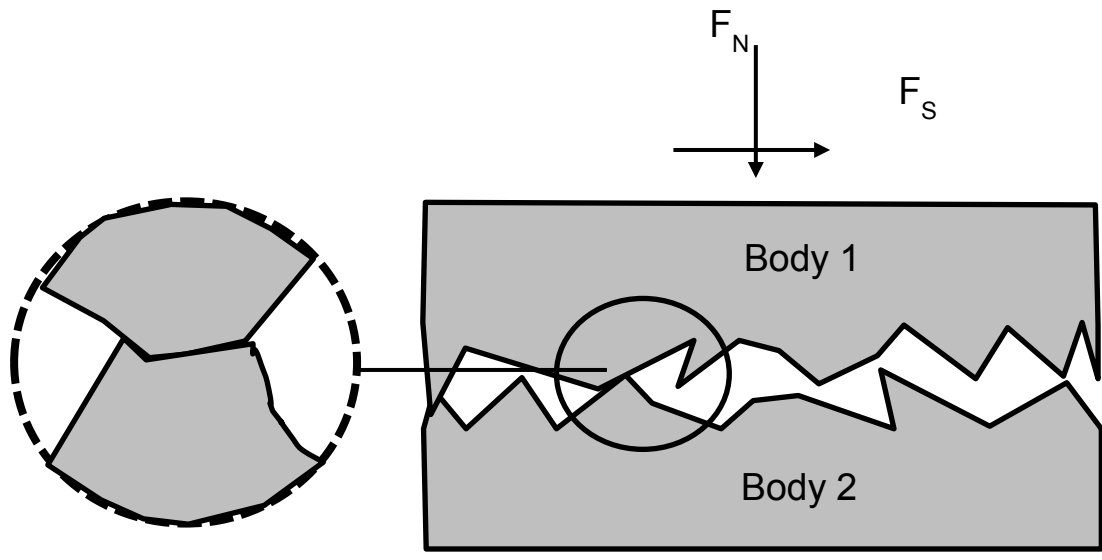
Figure 2. Contact mechanics of articulating surfaces

During the initial phase of dynamic contact, the tangential force reaches maximum level. As the relative force gradually increases, the resistance force of the softer material is shifted in front of the opposing asperity, causing unloading of force between the surface and the hard asperities. The maximum tangential force also increases the penetration depth, thereby increasing the real contact area. As the hard asperity kinetic motion increases, material detaching from the surface accumulates, providing support to the hard asperities to overcome static contact.
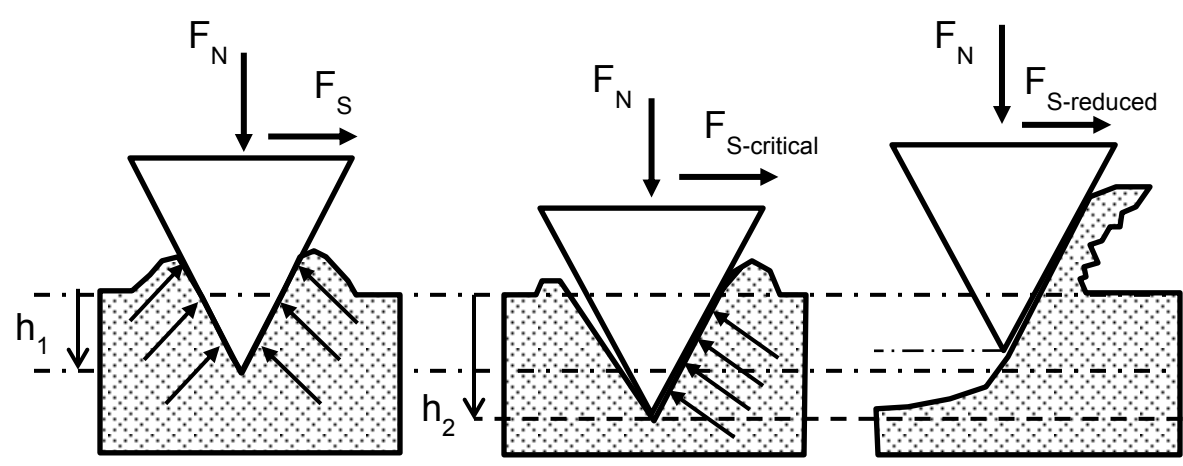
Figure 3. Schematic of the 3 stages of contact

The support of the materials accumulated onto the hard asperities reduces the tangential force in the sliding direction. The accumulated material reduces the amount of material required to be sheared as compared to the earlier stages of sliding [76]. The irregularities in height distribution of the contacting asperities can contribute to the effect of sliding causing the removal of material at small distances. The number of asperities in contact decreases as the relative motion transitions from static to dynamic. The generation of wear particles is caused by the shearing force of the harder asperities, in turn decreasing the real contact area at localized spots.

2.3.2 Wear Equations

The earliest theories of wear are based on the nature and number of local encounters between two atoms, one atom from each surface, in sliding/rubbing contact leading to the generation of wear particles supported by Holm (1946); Burwell and Strang (1952). In 1952, Archard proposed that wear phenomena occur between numerous asperities in contact [77]. Overall, the wear theories are based on the fact that wear is proportional to the apparent contact area and applied load [77]. The most commonly used equation in tribology is the Archard wear equation shown in equation (1).

$$V = KA_r x = K\frac{F_N x}{H} \qquad (1)$$

$$\dot{W} = \frac{V}{x} = K\frac{F_N}{H} = kF_N \qquad (2)$$

where V is the wear volume (mm^3); K is the Archard coefficient, which is a property of the system as a whole and not of just one material, A$_r$ is the real contact area, (mm^2), x is the sliding distance (m), F_N is the applied normal load (N), H is the Vickers hardness (Pa) of the softer material, $\dot{W}$ is the wear rate (mm^3/m); and k is the specific wear rate.

Equation (2) describes wear rate as wear volume per sliding distance. The rate of wear changes due to the repeated contact process under constant load and velocity [75]. Wear rate tends to be high during the initial phase, but tends to decrease upon reaching steady state. The change in wear rate can be contributed to the wear mechanism. Several wear mechanisms can be activated during the sliding process.

2.4 Type of Wear

Wear can be categorized based on the condition of the environment, type of wear motion, the surface topography, material-pair interaction, and other factors that may influence the material's wear behavior. In the literature [75], there are three types of wear: mechanical, chemical, and thermal.

2.4.1   Mechanical Wear

Mechanical wear is the result of the loss of material due to mechanical processes such as deformation and fracture. Deformation processes contribute to the majority of wear in ductile materials. Fracture contributes to wear in brittle materials. Wear mechanisms identified with mechanical wear are abrasion, adhesive, delamination, and fatigue wear [75].

2.4.2   Chemical Wear

Chemical wear is the degradation of materials due to the growth rate of chemical reaction film influenced by the friction from mechanical processes [75]. Chemical wear is also known as corrosion. Corrosion, combined with mechanical surface interaction in tribological contact, leads to wear known as tribocorrosion [68]. Corrosion processes can be accelerated due to the removal of the corrosion product that simultaneously destroys the material's protective layer [78].

2.4.3 Thermal Wear

Thermal wear is characterized by localized frictional heating and surface melting due to mechanical processing, resulting the loss of material. Wear that occurs at high temperature is known as diffusive wear. Thermal wear of brittle materials is caused by thermal shocks and fractures [75].

2.5 Wear Mechanisms

2.5.1 Abrasive and Adhesive Wear

Abrasive wear is caused by the tribological contact of hard asperities pressing against a soft surface that penetrates and removes or displaces material from the worn surface. Abrasive wear is a rapid and severe form of wear that can lead to a rise in costs if not properly tamed[76]. The asperities on the harder material make tribological contacts with the asperities on the softer material under an applied load, generating plastic deformation. The surface topography of abrasive wear shows a series of long grooves that is parallel to the sliding motion, and the formation of cracks. The rate of generation of abrasive wear particles is 2-3 orders of magnitude larger than adhesive wear particles [79]. New asperities are formed on the surface of the softer material after being subjected to wear [80]. Abrasive wear leads to ploughing, fatigue, cutting, and cracking on the micro-level due to the mechanical interaction of the surfaces asperities in contact. This can lead to the elimination of chemical reaction layers such as oxide films [76, 81-83]. Abrasive wear is commonly found in material pairs with dissimilar hardness.

Adhesive wear occurs between the asperities of two touching surfaces resulting in welding of the asperities [78, 84]. When relative motion occurs, a plastic shearing force is generated, breaking the adhesive bonds of the softer and deformed asperities. The newly generated wear particles adhere to the harder opposing surface. In other words, the softer

material generates a transfer film on the surface of the harder material. Wear particles adhering to the opposing surface eventually gets loosened, generating three-body abrasive wear between the opposing surfaces.

True adhesive wear has been found under dry conditions mostly with metals of similar hardness. This wear mechanism is not dominant in the lubricated conditions. This type of wear develops on a small scale. According to the literature [79], adhesive wear volume, V, is described by the Archard's wear equation:

$$V = \frac{kF_N x}{3H} \qquad (3)$$

where κ is the probability of generating wear debris. κ is equivalent 3 times the term K in of the abrasive wear equation and represents the system property, not a material property. This equation is based on the assumption that wears occurs by shearing of the true contact area between two contacting surfaces and that the true contact area is a function of the contact stress yield point of the surface of the softer material (the mean contact yield stress is about three time the tensile yield point) [78].

2.5.1.1   *Two-Body and Three-Body Abrasion Wear*

Two-body abrasion occurs due to the hard protrusions or asperities on one surface ploughing or gouging the softer surface. Two-body abrasive wear can also be viewed as an adhesive wear mechanism activated by adhesive shearing and transfer on the harder material surface as shown in Figure 4. Three-body abrasive wear is produced by hard particles that are free to roll or slide between the two surfaces in relative motion as shown in Figure 5. During sliding wear, the hard asperities cause plastic deformation on the surface of the softer material. This can generate third bodies in the form of particles. Wear debris can either adheres to the hard

counter-face and continue to contribute to abrasion wear, or become loose wear particles that either leave or merge with the worn surface. Wear particles can become entrapped in the worn surface, changing the nature of contact.
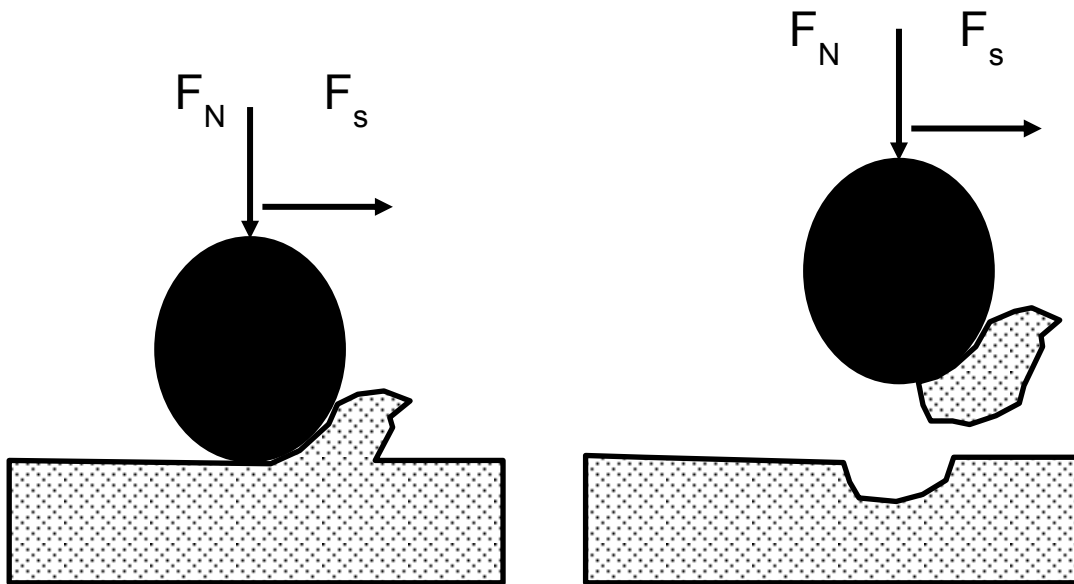

Figure 4. Two-body abrasive wear (adhesive wear)
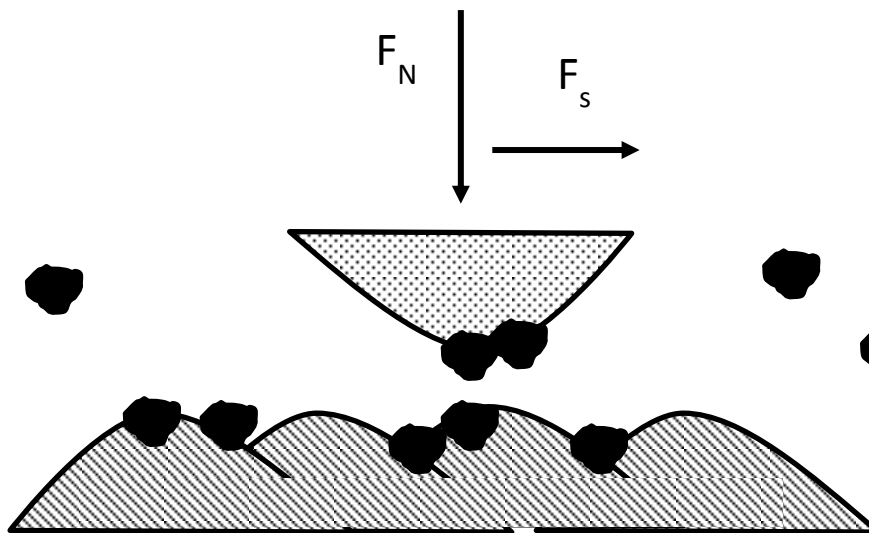
Figure 5. Three-body abrasive wear

2.5.2   Fatigue and Delamination Wear

Fatigue wear is a wear mechanism under repeated sliding, rolling, or impact where the material's surface experiences cyclic shear stresses or strains that initiate cracks and induce wear in the region shown in Figure 5 [81-83]. The increase in applied normal load results in plastic deformation that causes extensive damage to the materials. The contact area can be conforming or non-conforming. Using a Hertzian contact theory, the near-surface stress field can be estimated in elastic materials [79]. According to [81-83], delamination wear occurs when plastic flow nucleates and promotes the growth of subsurface cracks that propagate parallel to the surface, before extending out to the free surface to form platelet-like wear particles. Delamination can occur simultaneously during the fatigue wear process. The fatigue wear that is occurring on the material's surface initiates cracks in the worn region and as the cracks continue to grow and connect with other propagating cracks, materials are released from the surface in sheet-like shapes as illustrated in Figure 5.

Figure 6. Schematic of fatigue and delamination wear mechanism

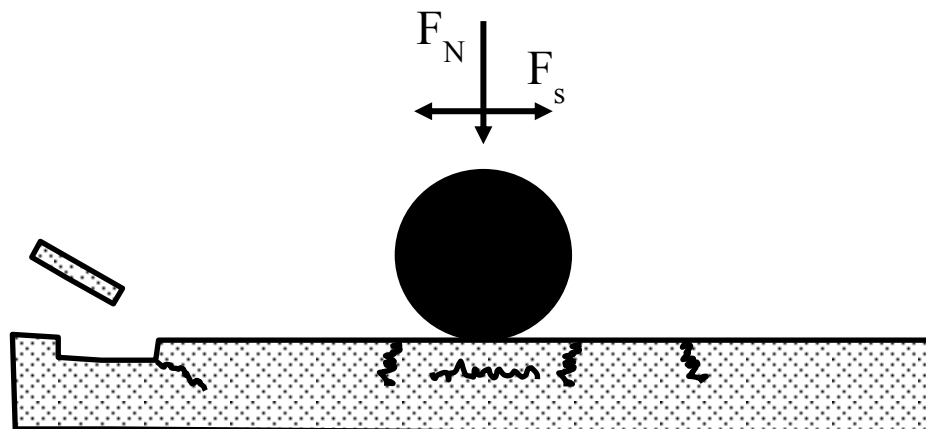**2.6 Friction**

Friction is the force that resists the relative motion between touching solid surfaces in contact, fluid layers and other elements. According to ASTM Standard G40-13, friction is a resisting force tangential to the interface between two bodies when, under the action of an external force, one body moves or tends to move relative to the other. During contact, the high asperities of the hard material press and deform the asperities of the softer material, creating a localized contact stress. The junction resists the tangential motion by the hard asperities in the form of ploughing or shearing of junctions of the softer materials.

Friction is an energy dissipation process that occurs in the initiation and continuation of relative motion of solid surfaces in tribological contact [76, 85]. The first two laws of friction were first proposed by Amontons in 1699. The first law of friction states that the frictional force is proportional to the applied normal load during sliding. In the fifteenth century, Leonardo da Vinci demonstrated that a wooden block would slide down a ramp with the same friction force no matter whether it stood on the end or on its broadest face [78]. The first law of friction is expressed in mathematical form as:

$$\mu = \frac{F}{N} \qquad\qquad (4)$$

where μ is the coefficient of friction, F is the limiting frictional force and N is the applied normal load. The second law of friction states that the frictional force is independent of the apparent contact area. The third law of friction, proposed by Coulomb in 1785, states that the friction force is independent of the sliding speed. This law refers to the kinetic friction that occurs during relative motion of surfaces in contact. The coefficient of kinetic friction is the ratio of frictional force to the normal as shown in equation (1). The force needed to initiate sliding is greater that

the force needed to sustain sliding. Energy is required for the contacting surface to go into motion and to maintain it. Energy is dissipated in the form of deformation or energy at the rubbing surface. In the presence of lubrication, the energy is dissipated by the movement of the fluid in the form of waves or heat transfer between the moving surfaces.

Friction has long been known to contribute to wear in medical devices [86]. For instance, failure in implant devices such as hip implants has led to device recalls. The failures were due to a mismatch in material and surface properties resulting in an accelerated wear rate that contributed to implant loosening and wear particles entering the surrounding tissues and blood system. These problems led to a major recall leading to the loss of billions of dollars in compensatory damages for the affected patients, who had to undergo revision surgeries.

CHAPTER 3

Materials, Experiments, and Methodology

3.1 Materials and Sample Preparation

During the pilot study, aluminum and pure Mg were evaluated with respect to wear properties. Aluminum and magnesium specimens were extracted from an aluminum bar and a magnesium billet, respectively. The magnesium billet for the pilot study was supplied by Goodfellow.

The materials used in the main study were pure magnesium and Mg-Zn-Ca-RE alloys. The pure Mg was supplied as ingot by US Magnesium. The MZCR was cast at NCAT. The MZCR was cast in a 20 x50 x 100 mm^3. From Mg (99.97%) and Mg-Zn-Ca-RE three main fabrication states for: as-cast (pure Mg) and T4 solution heat-treated (MZCR) and extruded (extrusion ratios 10 and 50 for both materials. Both materials were cast at 350°C and solution heat treatment was done at 510°C. Pure Mg was extruded at 350°C and MZCR was extruded at 400°C (with extrusion ratios of 10 and 50) at a extrusion rate of 1 mm/s. Extrusion resulted in rods of diameters of 12 and 5 mm, respectively. The extruded specimens were cut using a diamond disc precision cutter. Cutting perpendicular and parallel to the specimen's extrusion direction resulted in wear test specimens that were shaped like disk (diameter and thickness) and half cylinder (diameter and thickness), respectively.

Wear test surfaces were first polished using 9 μm, 5 μm, 3 μm, and 1 μm alumina using lubricant. Using a Wyko RST-500 optical profiler, the average surface roughness of the Mg and MZCR specimens were measured to be about 0.15 μm and 0.18 μm respectively. The specimens were etched with picric acid to reveal and add contrast to the grain boundaries. Specimens were

cleaned with isopropanol before and after wear testing in order to analyze the changes in material's microstructure.

3.2 Microtribometer

A CETR-UMT-2 microtribometer was used to conduct wear tests to assess the wear and friction characteristics of the aluminum, Mg and MZCR alloys as shown in Figure 7. The microtribometer consists of several components and is used to analyze the wear behavior of the material being tested. It contains an upper and lower testing system mechanism.
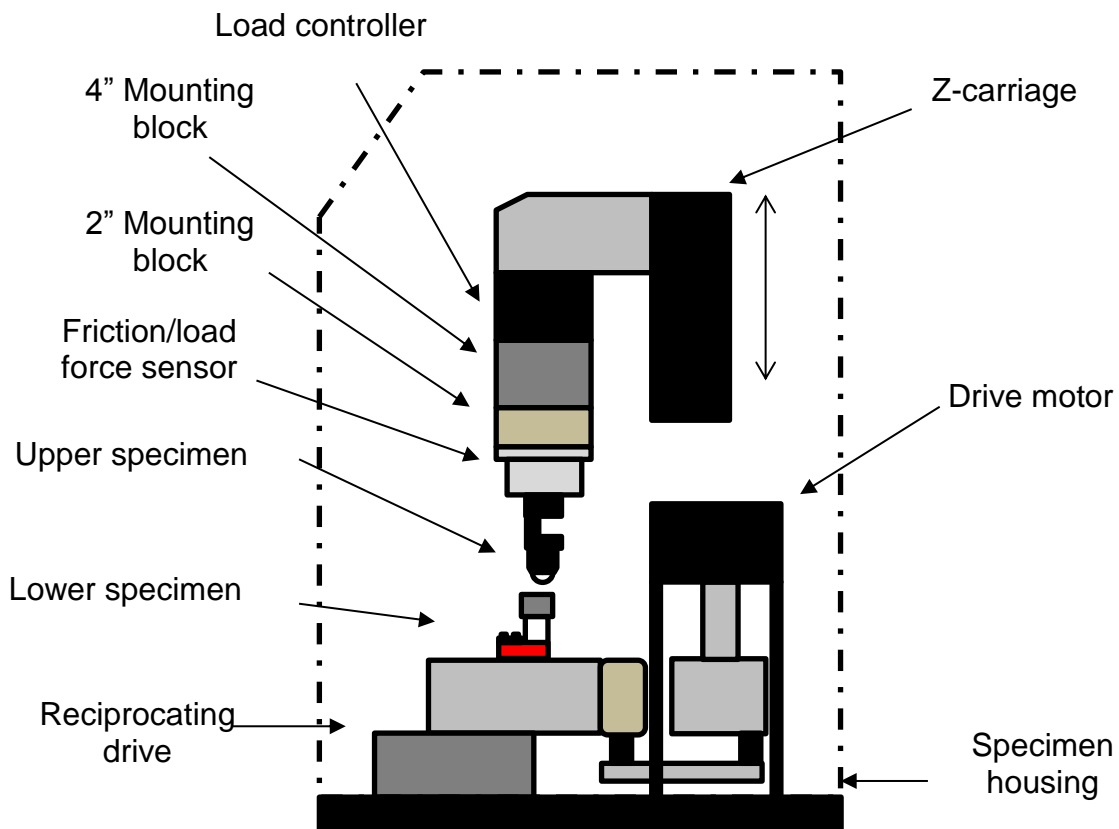

Figure 7. Schematic of microtribometer in reciprocating configuration

3.2.1   Upper Subassembly

The microtribometer upper testing system consists of a z-carriage with vertical motion capability that supports a load controller and friction/normal load sensor. The load cell controls

the amount of normal load applied on the lower specimen. The friction/load sensor used in this study has a maximum normal load range of 10 N. The sensor monitors the applied normal load and friction force generated during testing. Another component of the upper specimen is the suspension and the specimen holder. The suspension is used to help regulate the normal load applied on the test material. The specimen holder is used to hold a counterface in the form of balls, pins, needles, and micro-cutting blades.

The pilot study used a tungsten carbide spherical counterface as the upper specimen during testing. During the main study, the upper specimen was a sapphire spherical counterface. The sapphire and tungsten carbide sphere geometry consists of a diameter of 3.97 mm. The Vickers hardness of the sapphire and tungsten carbide are of 2500 and 2242, respectively. The upper specimen was cleaned with an ultrasonic cleaner in distilled water solution for thirty minutes to remove previous wear debris.

3.2.2   Lower Subassembly

The lower components of the microtribometer consist of a horizontally reciprocating drive mechanism and the test specimen (Al, Mg and Mg-Zn-Ca-RE). The reciprocating drive is one of the tribometer's three available configurations of wear testing. Pin-on-disk and block-ring are the other test configurations. All three configurations are designed to investigate sliding wear. Reciprocating wear was the configuration used in this study and will be discussed in the next section.

The reciprocating wear test, also referred to as ball-on-flat sliding wear is shown in Figure 6. The upper specimen is the ball-shaped counterface and the lower specimen is the flat-surface of the material under investigation. The ball specimen is rigidly mounted to the force sensor and during the initial phase of testing, the ball is pressed normally onto the flat specimen.

Normal load is applied vertically through the ball specimen that the flat specimen reciprocates horizontally against, creating wear on the surface. When the sphere contacts the flat surface, the mass of the sphere is supported at a localized point. This creates stress at the point of contact and causes elastic deformation that increases the size the real contact area until the stresses decrease below the elastic limit. When the stresses due to the normal load approach the elastic limit of the flat material, plastic deformation occurs [78]. Reciprocating wear is a dynamic version of a hardness test using similar contact conditions. The similarity in contact conditions and mechanics show the important role that penetration hardness plays in affecting wear and friction behavior. The sliding of the lower specimen is controlled by the tribometer reciprocating drive. The reciprocating drive controls the sliding velocity and the direction of motion.
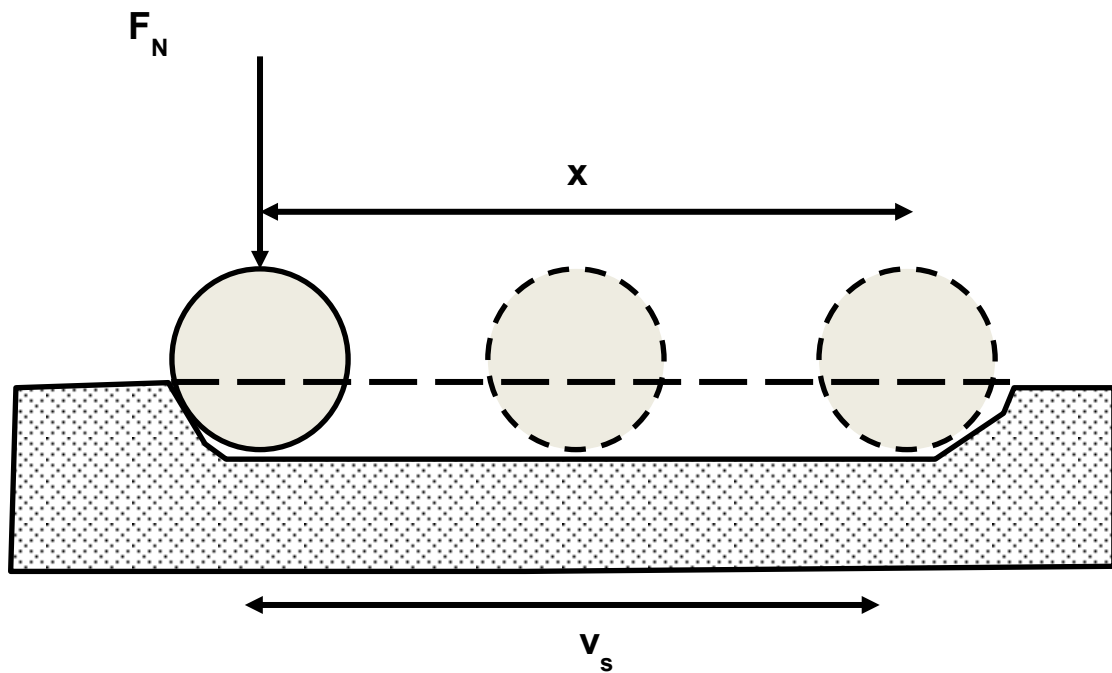

Figure 8. Schematic of the reciprocating ball-on-flat testing configuration

Three kind of wear tests were conducted in this study, shown in Table 2-3. The first wear test was conduct in the pilot study on Al and Mg using a tungsten carbide sphere for 6 minutes at 72 cycles per samples as shown in Table 2. The normal load applied during testing were 0.5 N, 1.0 N, 1.5 N, 2.0 N. The purpose of this was comparing the wear properties of Al and Mg to ensure repeatability and accuracy of the wear technique. The wear property of magnesium was further analyze based on the grains with the Mg microstructure

Table 2. Testing parameters of the pilot wear testing

Normal load (N)	0.5-2.0	Oscillation frequency (Hz)	0.2
Testing material #1	Al	Testing material #2	Mg (99.97%) (Goodfellow)
Number of passes	144	Number of replicates	2
Test duration (s)	360	Temperature (^{o}C)	25
Upper specimen counterface	WC sphere dia. 3.97 mm	Environment	Dry

The main study wear tests were conducted for 10 minutes at 120 cycles per samples. The stroke length was altered to suit the size of the sample and alignment of the tribometer stage was carried out to ensure that the upper specimen was normal to the lower specimen surface. Loads applied during testing are as follow: 0.5, 1.0, 1.5, 2.0, and 2.5 N. The purpose of this wear test is to compare the wear properties of Mg and MZCR alloy.

Table 3. Testing parameters of the main wear test study

Normal load (N)	0.5-2.5	Oscillation frequency (Hz)	0.2
Test material #1	Mg (99.97%)	Test material #2	MZCR
Number of passes	240	Number of replicates	3
Test duration (s)	600	Temperature (^{o}C)	25
Upper specimen counterface	Sapphire Sphere dia. 3.97mm	Environment	Dry

Wear properties were analyzed for a) as-cast, and the extruded specimen in the b) longitudinal direction (ED), transverse direction (TD), cross-section (TD-ND plane) as shown in Figure 9.
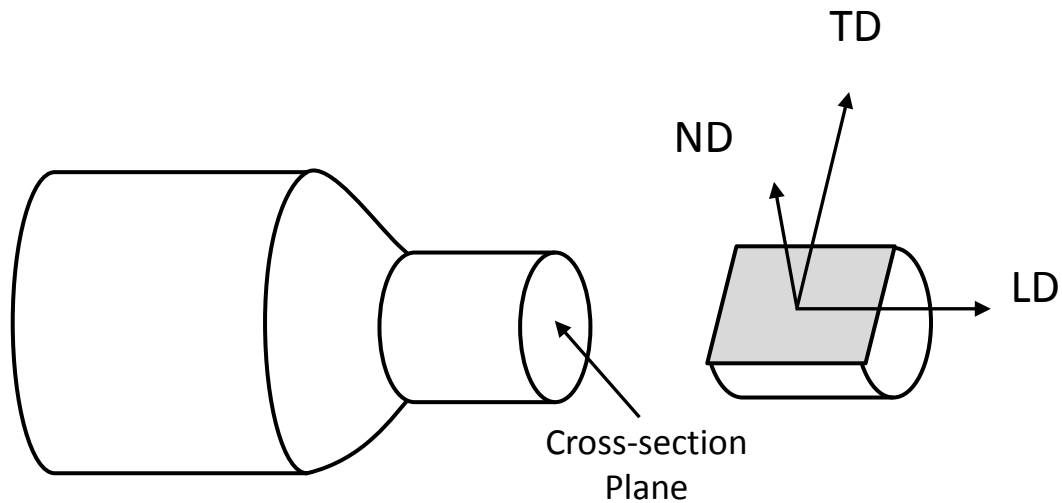

Figure 9. Schematic of extruded specimen's coordinate system

The frictional force, normal force, shear force, height/depth, and coefficient of friction were monitored and recorded by the microtribometer load cell and analyzed with the UMT-2

Viewer software as shown in Figure 8. The pilot study was replicated twice for each value of

normal load. The main wear study was replicated three times for each normal load value.
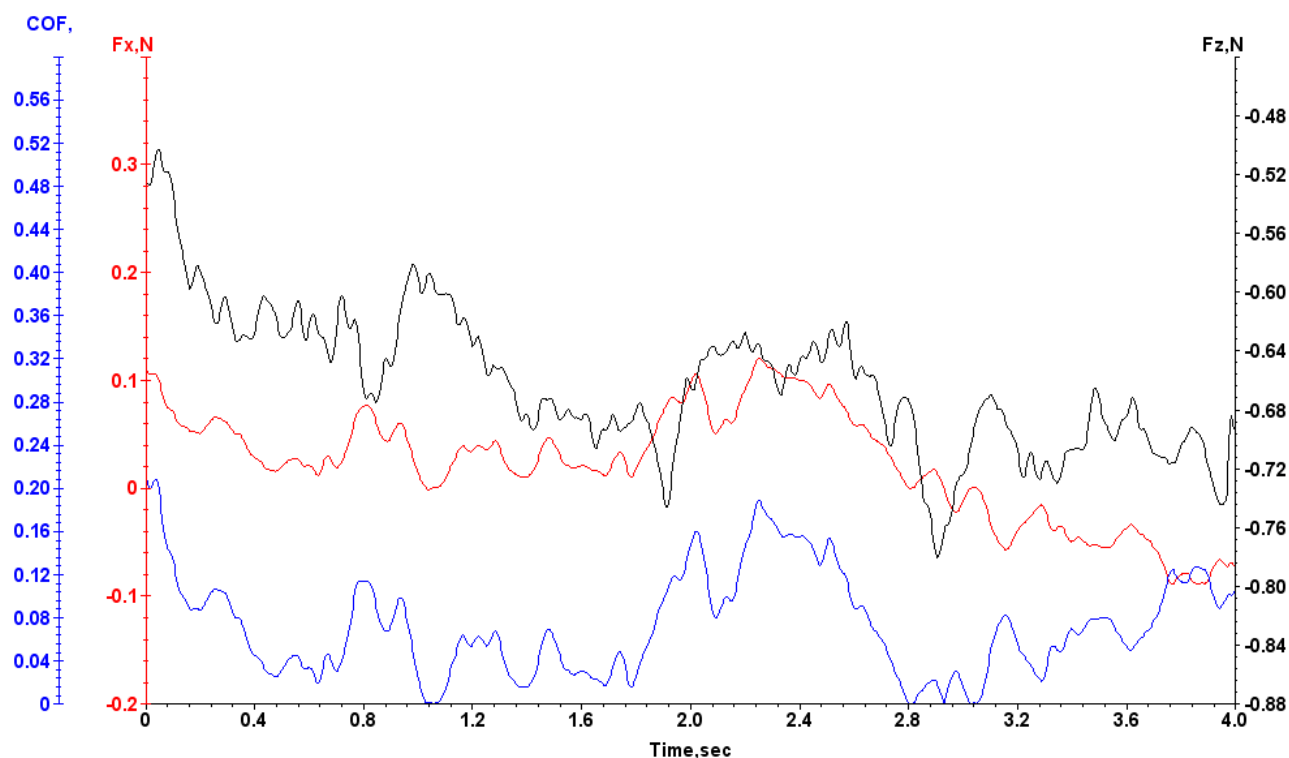

Figure 10. CETR UMT-2 Viewer software plot of forces and coefficient of friction

3.2.3   Specimen Alignment

Prior to wear testing, alignment of the specimen surface was done in order to get

sufficient traction between the upper and lower specimen. As mentioned in Section 2.3.1, the

material surface is composed of small asperities. During polishing, the asperities of the specimen

are in tribological contact with the asperities of the polishing agent (alumina) and undergoing

plastic deformation. Since polishing is a form of abrasive wear, material is being removed from

the surface. The materials being removed either get dispersed in the lubrication solution, or

adhere to the polished surface. The wear debris from the specimen adheres to the polishing agent

removing uneven amount of materials from the surface, and causing irregularity in the sample surface.
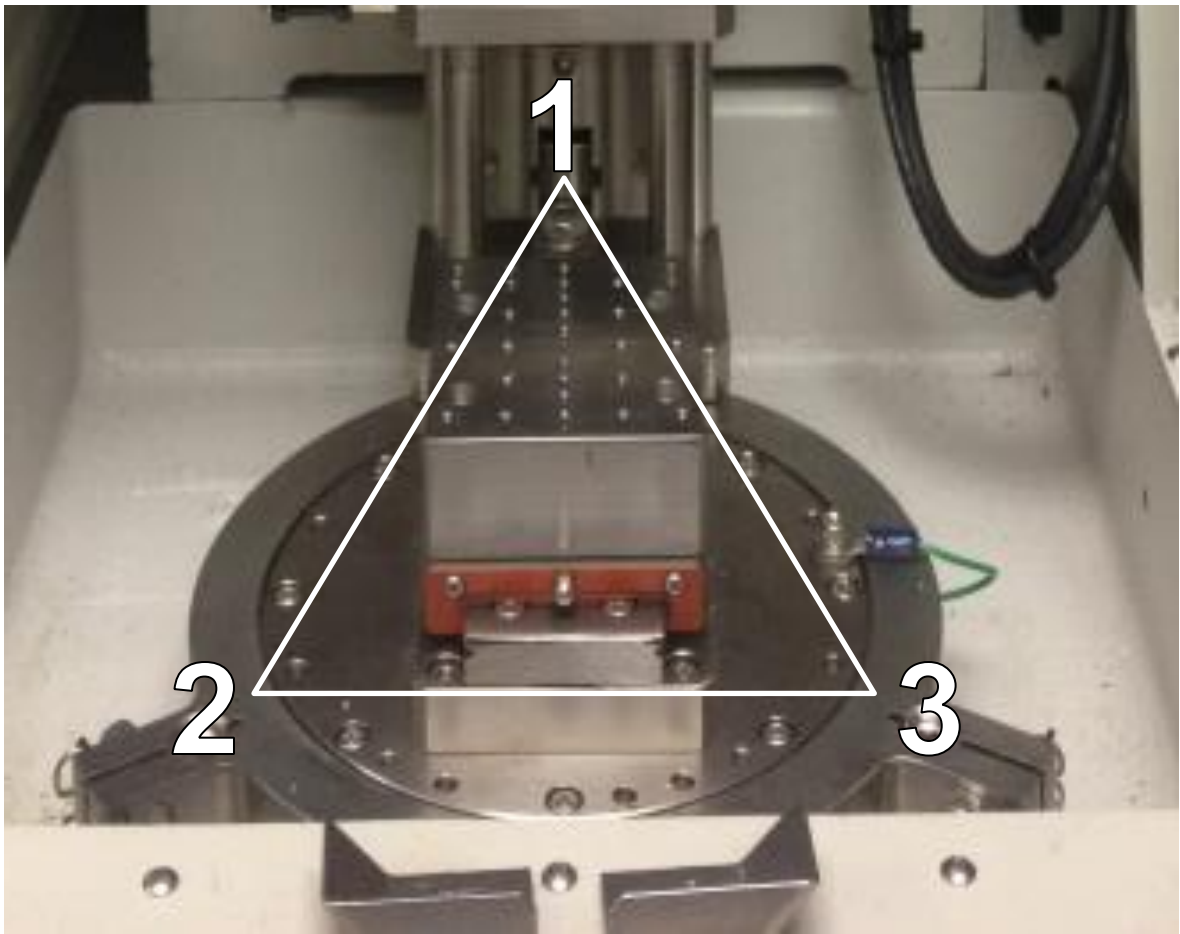
Figure 11. Schematic of the specimen alignment procedure

During alignment, the sample is mounted onto the lower specimen drive. The upper specimen is manually lowered onto the middle of the specimen surface in triangle formation shown in figure 9. The specimen height is adjusted at point 2 and 3 based on the first measure at point 1. No adjustment was made to point 1 since the specimen drive is attached in that area. Adjusting point 2 and point 3 with respect to point 1 will ensure that the surface of the sample is perpendicular to the normal load. The alignment of the stage would eliminate the misalignment between the counterface and specimen.

3.3 Microindentation

Microindentation tests were carried out using a LECO M-400-H1 microhardness tester and following the ASTM Standard E384-11 in order to investigate the hardness of the magnesium and MZCR alloys. The purpose of the microhardness test is to measure the material's resistance to plastic deformation by an indenter. Measurements of the permanent indents with the assistance of an optical microscope and Image Pro 6.0 imaging software are used to determine the hardness of the sample. Microindentation samples were prepared under the same conditions as the wear samples. Cross-sectional and longitudinal sections were tested. The microindentation tests were conducted for thirty seconds per indent using an indentation force of 300 gf (2.94 N) for the extruded sample and the as-cast material, with indent-to-indent spacing of at least 30 μm. At least 20 indentations were carried out per sample. A Vickers indenter, which is a pyramidal-shaped diamond indenter (with face angle of 136°), is pressed against the surface under with the 300 gf normal load, forming a micro-sized imprint.

The shapes of the indents varied between Mg and MZCR. Most of the indents made on the MZCR surface were well-defined, with a rhombus shape as shown in Figure 12. The indentation of the pure Mg surface resulted in distorted imprints. The hardnesses for the Mg and MZCR were calculated by two different equations based on whether the indenter was a well-defined rhombus or not. The well-defined indents were estimated based on the mean diagonal of the indents as shown in Figure 12. According to the ASTM Standard [87] the hardness equation is as follows:

$$HV(GPa) = 18.186 \left(\frac{P}{d^2}\right) \tag{5}$$

Hardness for distorted indents was calculated based on the area estimated by the Image Pro 6.0 software and entered into the following equation:

$$HV\ (GPa) = 9.093 \left(\frac{P}{A}\right) \tag{6}$$

where P is the load applied in gram-force (gf), d is the mean diagonal length (μm) of the well-defined imprint, and A is the surface area (μm^2) extracted from the Image Pro 6.0 software in the case of irregular imprints as shown in Figure 13.
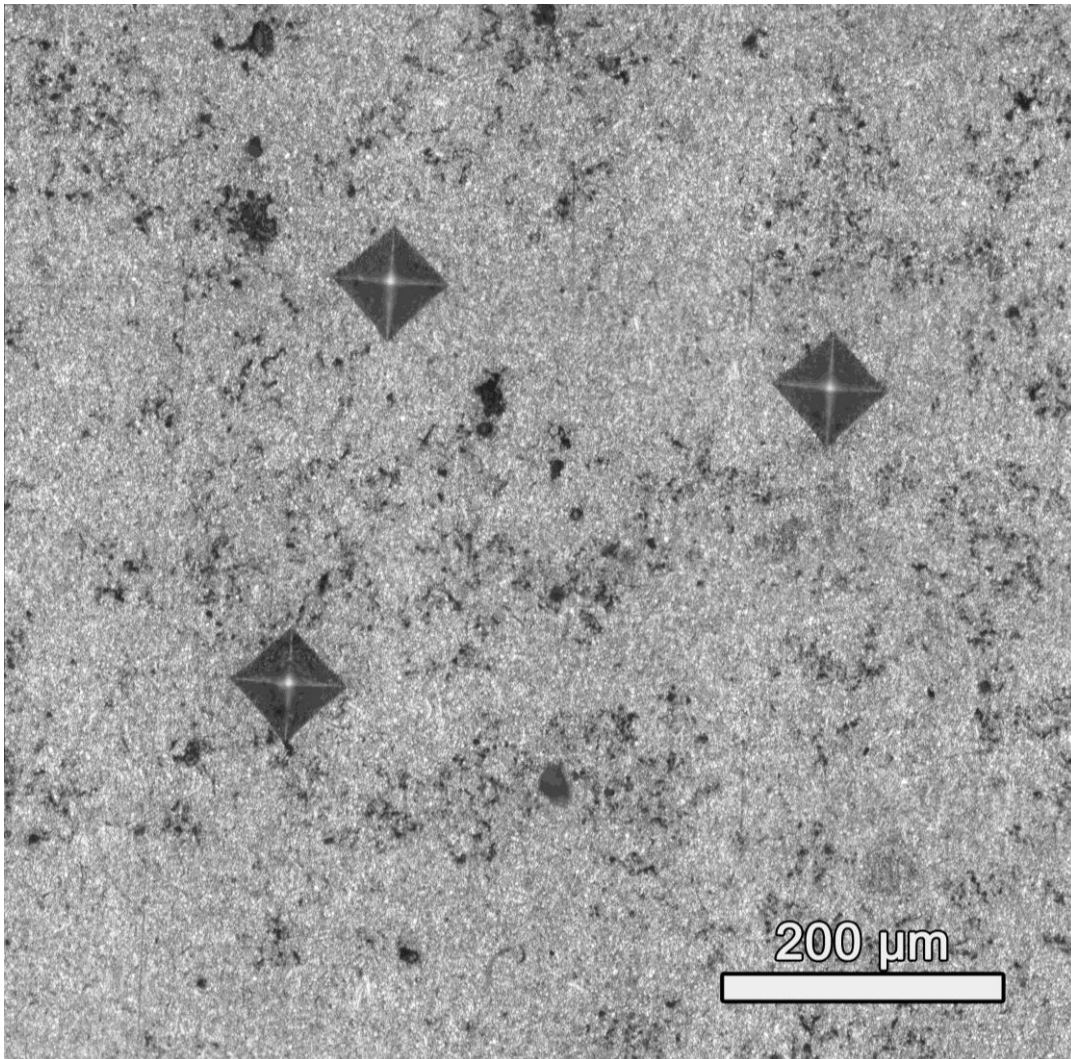

Figure 12. Well-defined regular indentation on MZCR-ER50 cross-section

The coefficients in equations 5 and 6 are based on the shape factor listed in the ASTM standard for the square-based pyramid-shaped indenters multiplied by the conversion factor of

9.807×10^{-3} N/gf. As mentioned earlier in this section, the second equation is based on the

projected area. The area of a regular rhombus of diagonal length is shown in the equation below:

$$A = \frac{d^2}{2} \qquad (7)$$

According to the equation, d^2 is equivalent to two times the area of the indents.

Substituting the 2A into equation 5 will divide the coefficient in half, leading to the equation 6.

Well-defined indents were on the surfaces of the MZCR-ER10 and MZCR-ER50 in both the

cross-sectional and longitudinal planes. Distorted imprint were seen on the surface of the T4

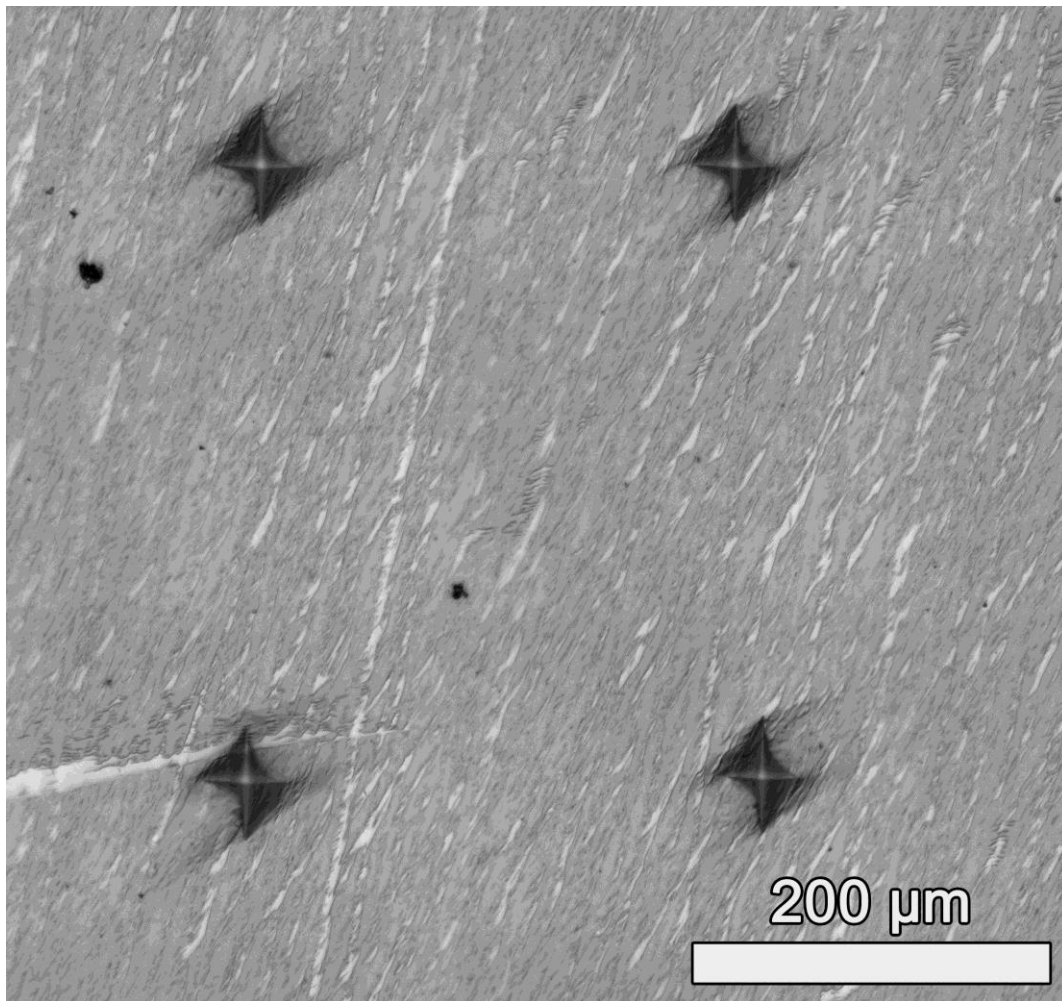solution heat-treated MZCR specimen and the as-cast and extruded Mg specimen.

Figure 13. Distorted indentation shapes seen on as-cast pure Mg

3.4 Materials Characterization

3.4.1   Optical Profilometry

Surface analysis was conducted on the magnesium and magnesium alloys using a *WYKO RST Plus* non-contact optical profiler, shown schematically in Figure 14. The optical profiler was used during this study to analyze the surface roughness of test specimen prior to wear testing. The optical profiler uses a surface profiling system capable of measuring smooth and rough surfaces using two modes of white light interferometry. The optical profiler consists of the following components: light source, neutral density filter, beam-splitter, PZT transducer, microscope objective, Mirau interferometer, detector array.
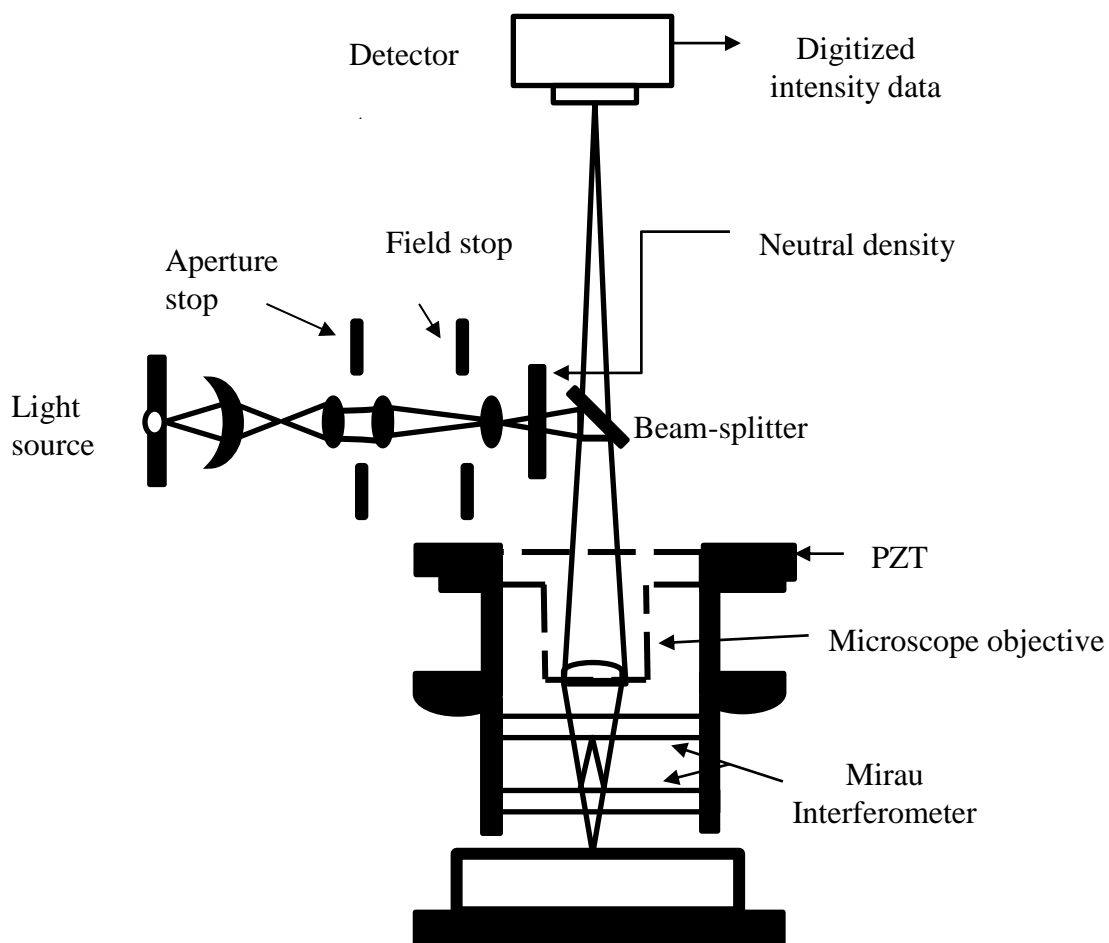

Figure 14. Schematic of optical interference microscope

The first mode of white light interferometry is phase-shifting interferometry (PSI). PSI mode is used to measure smooth surfaces at a maximum height of 160 nm with vertical resolutions of 3 Å for a single measurement, and less than 1 Å for average measurement for multiple scan [88]. Conducting average interferometric measurements will reduces noises occurring during measurements and from the surrounding environment. In PSI mode, white light is directed toward a red filter with a narrow-bandwidth. It passes through a beam-splitter which divides the incident beam into two parts, reflecting the beam off a reference surface and a beam that reflects off the sample, passing through the microscope objective. Once the two beams reflected from the reference and sample surface recombine, the beams form superimposed images of the measured surface with an interference fringe pattern on the detector array [89]. During PSI measurement, the piezoelectric transducer moves the mirror linearly along the sample in small increments to generate several phase shifts within the optical path of the measured surface and the reference mirror, generating changes in the interference pattern. The intensity of the phase shifts is recorded by the detector array, then the information is converted into phase data.

The second mode of white light interferometry is vertical-scanning interferometry (VSI). VSI mode is used for the measurement of rough surfaces and steps with roughness ranging from 160 nm - 500 μm, with a resolution of 3 nm for single measurement and < 1 nm for an averaged measurement. In VSI mode, a beam of unfiltered white light is directed through a microscope objective onto the sample surface. The beam splitter reflects half of the incident beam onto a reference surface. The reflected beams from the reference and sample are recombined at the beam splitter to form fringes. During the measurement, the interferometric objective in the reference arm moves vertically, scanning the surface at varying heights. The linearized PZT

precisely controls the motion because the short coherence length of the white light generates interference fringes at shallow depths at various focus positions.

Title: Pure Mg Grains
Note: Grains 3,7,8
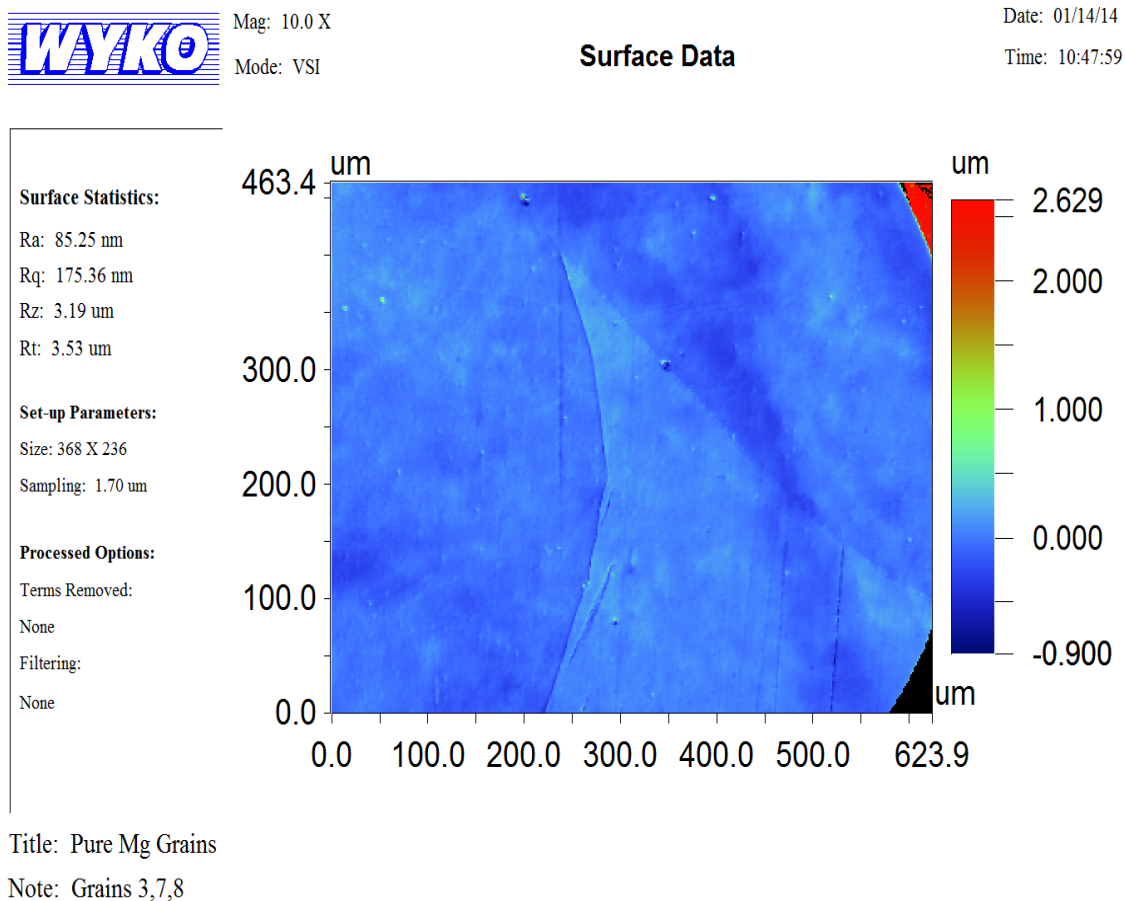
Figure 15. Optical profiler surface data analysis of pure Mg from main study

Figure 15 displays the surface topography information of pure Mg (99.97%) supplied by U.S. Magnesium used in the main study. Surface parameters such as surface average roughness (R_a), root mean square (RMS) roughness (R_q), maximum height of the profile (R_t), and average maximum height of the profile (R_z) describe the height of the asperities on the magnesium surface. The WYKO RST surface analysis program has the capability to analyze the surface profile in two-dimensional and three-dimensional modes.

3.4.2 Optical Microscopy

The microstructures of the magnesium and MZCR alloy were analyzed using the Zeiss Axio Imager Upright Microscope. Bright-field optical microscopy was used to characterize grain and surface morphology before and after wear testing. Image Pro 6.0 imaging software was used to analyze the optical micrographs in order to measure grain size, length of wear track and to analyze the indentation for hardness measurements.
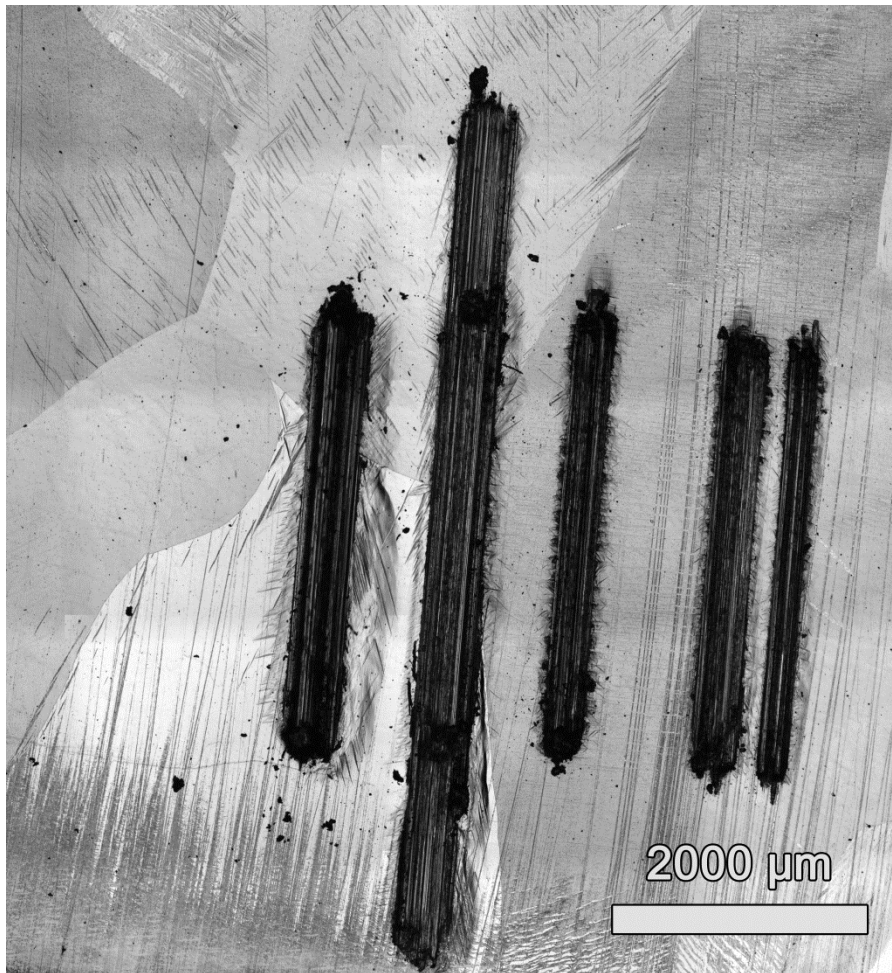

Figure 16. Optical micrograph of the worn surface of pure Mg

The stroke length of the wear track was extracted from Image Pro 6.0 imaging software. The stroke length of each test determines the length of the wear track. The stroke length was varied from test to test in order to accommodate the dimensions of the samples. The stroke

length measurements were used to calculate the total sliding distance per wear track according to the ASTM Standard G133-05 [90]. The sliding distance was calculated as follows:

$$x = 0.02 \times t \times f \times L \qquad (6)$$

Where x is the total sliding distance (m), t = duration of the test (s), f = frequency (Hz), and L = stroke length (m).

3.4.3   Scanning Electron Microscopy

The Hitachi SU8000 Field Emission Scanning Electron Microscope (SEM) was used to analyze the surface morphology of the worn specimens, as shown in Figure 17. The SEM has a higher depth of field and greater resolution compare to the optical microscopy.
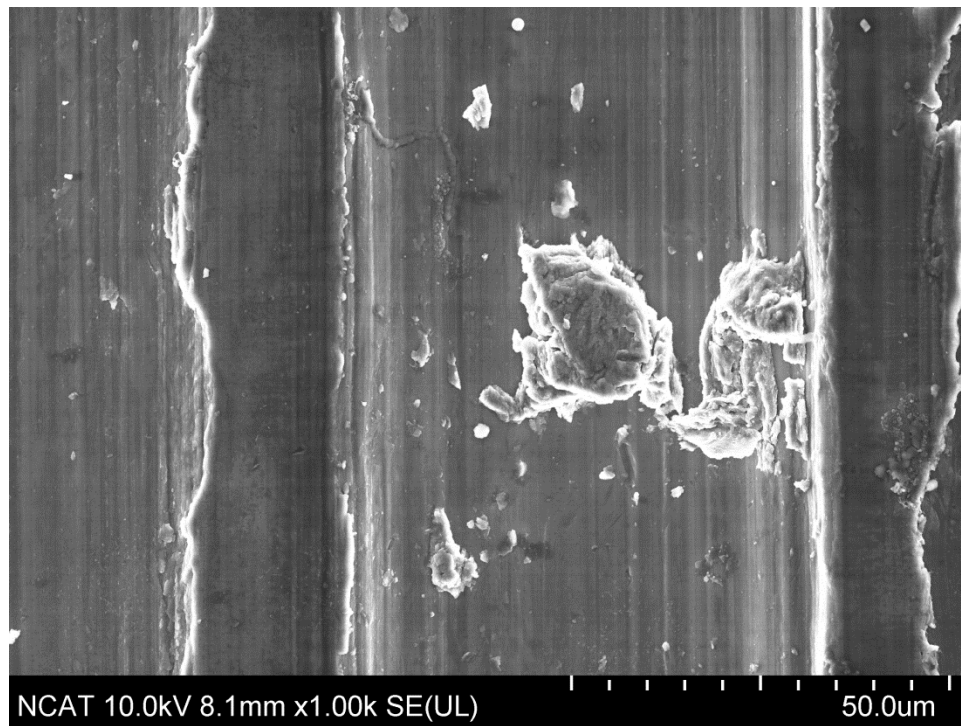

Figure 17. SEM micrograph of wear track

Scanning electron microscopy utilizes an electron gun that generates and accelerates free electrons to energies ranging from 1- 40 keV. The SEM focuses a beam of diameter about 10 nm on both sides of the sample. SEM images are produced by using a fine probe formed by this

beam to scan across the surface of the sample in a raster pattern. Raster scan is a rapid scan that moves point by point horizontally along the line scan (x-axis) from left to right across the specimen surface, collecting the signal intensity of the electron emitted by the surface. The line scan is followed by a stepwise slow scan that moves along the y-axis a predefined number of lines. The SEM utilizes two types of electromagnetic radiation generated from the collision of electrons from the incident beam and the specimen surface called secondary electrons (SE) and backscattering electrons (BSE). SE signals are the results of the incident electron beam colliding onto the specimen surface, knocking out secondary electrons from the atom's outer electron shell. SE imaging can display information on the surface topography of the specimen under investigation.
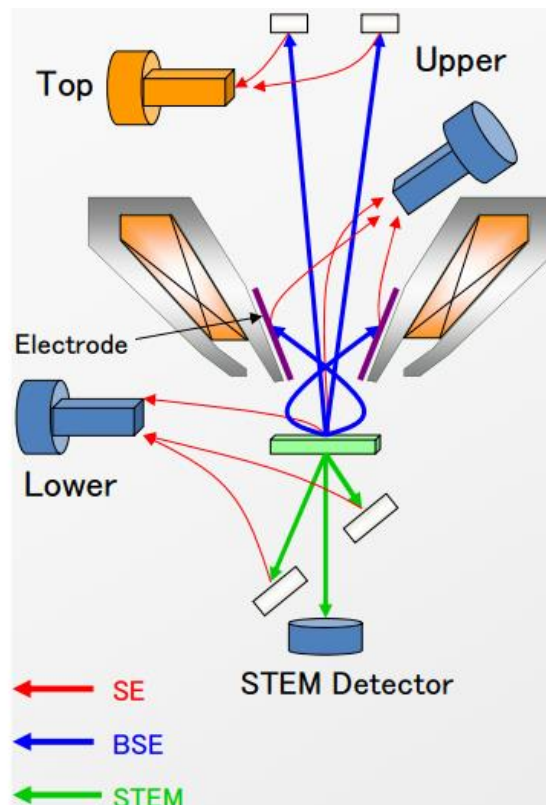

Figure 18. Schematic of the Hitachi SU8000 FESEM (Hitachi 2012)

Figure 18 shows the schematic of the Hitachi SU8000 detector system. The Hitachi U8000 FE-SEM SE imaging mode can display composition and crystal information (upper detector) and topography (lower detector). The BSE signals occur from the collision of incident beam with the specimen atom nucleus. The incident beam electron bounces back out as a backscattered electron. BSE imaging mode can display information on the relative atomic density and surface topography.

3.4.4   Mechanical Stylus Profiler

The morphology of the wear track was determined using an Alpha-Step IQ Surface Profiler. The surface profiler utilizes a stylus that scans across the surface, measuring various features of the surface topography such as roughness, waviness, area, depth, width, and step height. The specimen is placed on the rotary table. Measurement errors are minimized by placing a strip of double-sided adhesive tape to mount the test sample, ensuring that the samples remain stationary during the measurement scan. The Alpha-Step IQ Surface Profiler program uses a scan recipe to ensure the repeatability of the surface topography measurement. Recipes are used to establish measurement parameters prior to the scan. The parameters for the measurements made during this study are shown in Table 4.

The scan length of the measurements was adjusted based on the width of the wear track. Wear tracks from test under applied loads of 0.5, 1.0 and 1.5 N were scanned up to 500 μm in length. The wear track under applied load of 2.0 N and 2.5 N were scan up to 700 μm. A center bias adjustment was used to during the scan to optimize measurement of randomly-distributed surfaces. Multiple scans were used to measure the wear track to ensure repeatability. Ten measurements were taken along the length of the wear track at even increments per wear track. A total of 50 measurements were obtained per sample.

After scanning the surface, the measured profiles were analyzed in the Data Review tab of the Alpha-Step IQ Surface Profiler program. Measured profiles were leveled using a 2-zone operator. Profiles were leveled based on the flatness of the surface outside of the wear tracks. Profiles were individually extracted from the series to be further analyzed. The information extracted from the wear track profiles were wear track width (μm), depth (μm), and wear cross-section area (μm^2). Width of the wear track data can be extracted from the step height analysis using a 1-zone operator. 1-zone operator analyzes the height between the initial and final position of the wear track profile. Wear area and wear depth data are extracted from the Area of a Hole/Peak option located under the Studies tab in the software. The Area of a Hole/Peak option creates a graph and table of parameters with the purpose of evaluating the areas of the holes and peaks. Area and depth above and below the reference line is quantified under the Area of a Hole/Peak studies option.

Table 4. Mechanical profiler operational parameters.

Scan length (μm)	500 - 700	# of scan	10
Scan speed (μm/s)	20	Sensor range (μm)	400
Sample rate (Hz)	50	Adjustment	center bias

Wear volume (mm^3) was calculated according the ASTM Standard G133-05 [90]. Wear area was extracted from the Alpha-Step IQ Surface profiler software. The depth of the profile was also extracted from the program, using the step height function from the same software. The wear volume was calculated by multiplying the wear area (mm^2) from the stylus by the stroke

length (mm) obtained from the optical micrograph, as shown in equation (8). Stroke length was estimated from the optical micrograph.

$$V = A \times L \tag{8}$$

After obtaining the wear volume from equation (8), the wear rate can be computed. The wear rate can be calculated based on equation (2) by dividing the wear volume from equation (8) by the sliding distance from equation (6).

CHAPTER 4

Results and Discussion

In this chapter, the results of all the tests conducted are presented and discussed. The pilot study where the technique was developed of the technique is presented first, followed by the main study, where the wear performance of pure Mg and an ERC alloy are compared.

4.1 Pilot Study

This pilot study was designed to establish a suitable and systematic tribological technique for wear performance characterization with high precision and repeatability. Wear tests were conducted on Al and Mg under the conditions in Table 2 presented in Chapter 3. The Mg used in the pilot study was pure Mg (99.95%) in as-received condition from Goodfellow. Specimen alignment was carried out to ensure that the opposing counterface was properly aligned with the flat specimen, maintaining uniform contact. The technique established would then be applied to the main study in order to compare the behavior of Mg and with the MZCR ERC alloy.

4.1.1 Aluminum vs. Magnesium

Figure 19 shows the variation in wear rate based on the applied normal load. The specific wear rates of Al and Mg are 4.83 ± 0.04 mm^3/m and 10.28 ± 0.13 mm^3/m, respectively. The wear rate of Al was found to be significantly lower than that of magnesium. The wear data for both materials showed high precision and good repeatability, giving confidence in applying the technique developed here to the main study.
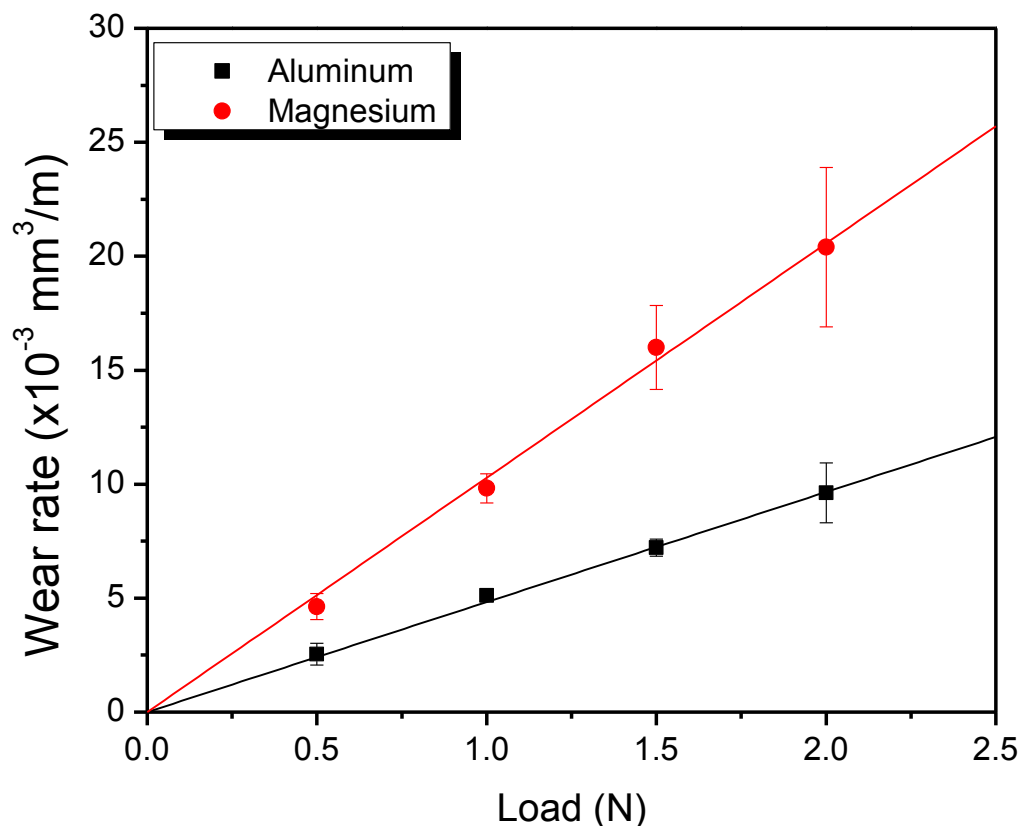
Figure 19. Effect of applied normal load on the wear rate of Al and Mg

4.2 Main Study Part I: Handling Outsized Grains in Pure Mg As-Received

After the pilot study, it was assumed that the wear technique developed would also work for testing of the materials in the main study. In the main study, the same wear technique was applied to pure Mg (99.97%) as supplied by U.S Magnesium. In this study, the stroke length was kept constant due to the large surface area. The average sliding distance in this study was about 0.48 m. After wear testing, the wear rate of Mg was found to have much greater scatter than measured in the pilot study. After a lot of puzzling over the probable cause of this large scatter, a microstructural study of the new Mg was done and compared with the old Mg from the pilot study.

The pilot study Mg (Goodfellow) had small grain size compared to Mg (U.S magnesium). On the other hand, it was found that the main study Mg (US magnesium) had outsized grains, with grain sizes to as large as 5 mm. The total number of grains in optical micrograph of the main study Mg was 9 grains. It was decided to do grain by grain wear testing for this material and five of the grains were involved in this wear test. The grains tested were grains 2, 3, 4, 6, 7, according to the microstructure map in Figure 20.
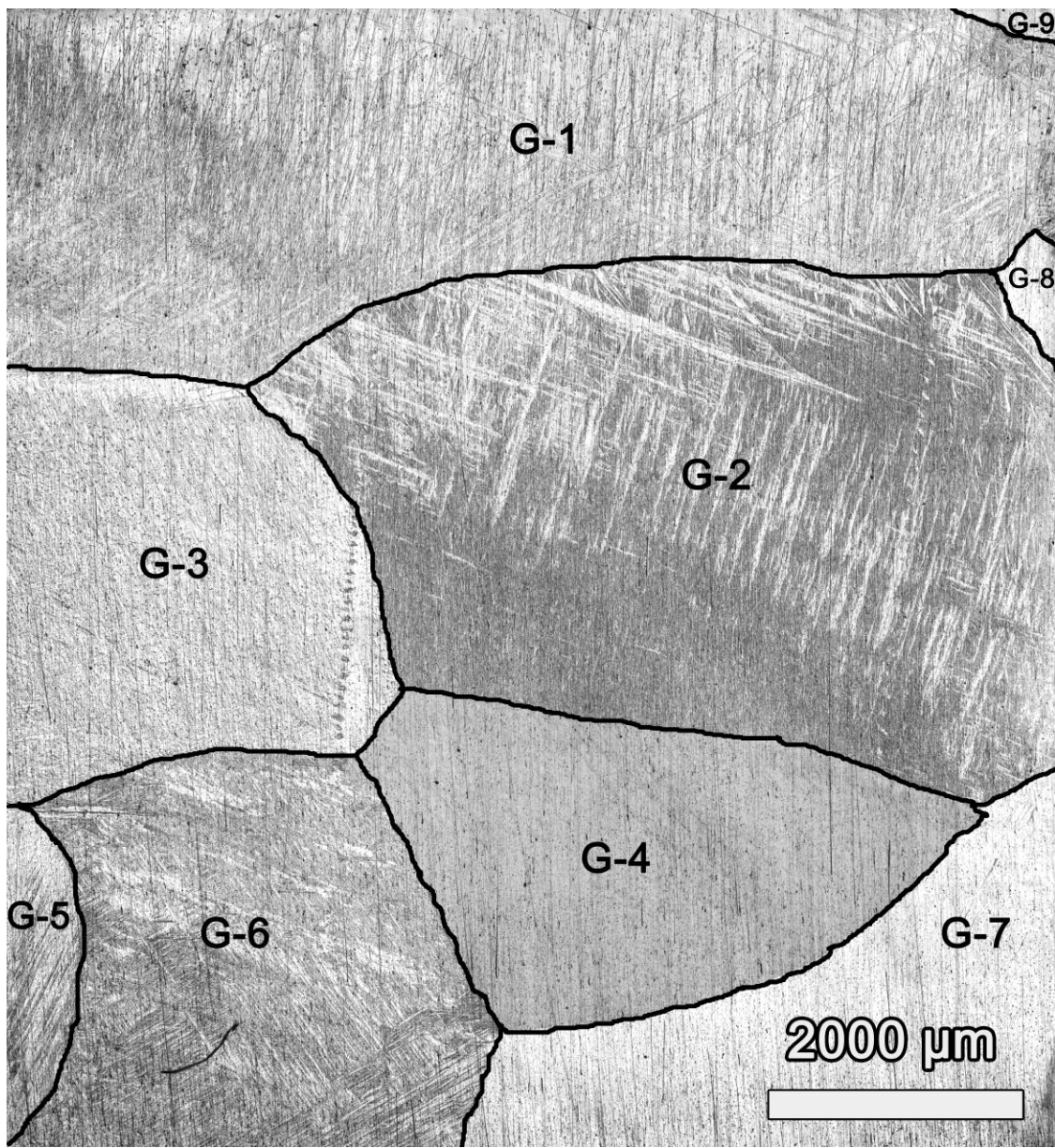

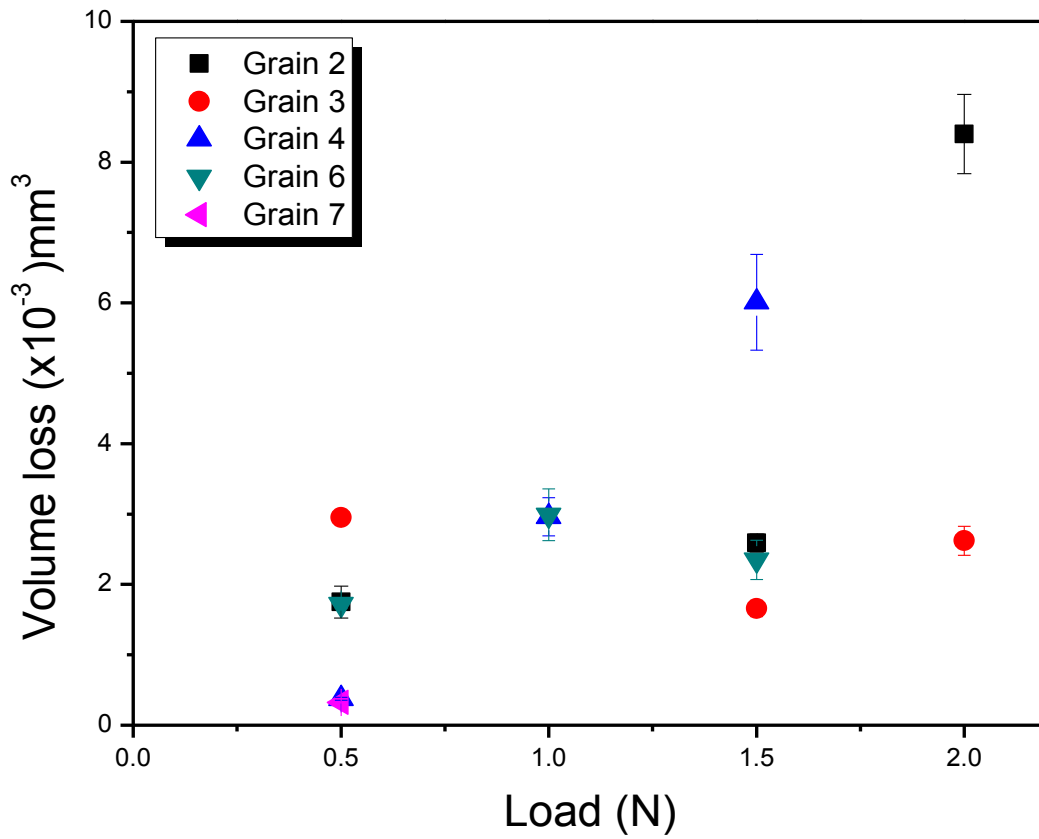*Figure 20.* Microstructure map - Mg sample (OM)

Figure 21. Wear loss volume vs. normal load of main study pure Mg sample

Figure 21 shows variation of volume loss of Mg with respect to the normal load applied

to various grains with in its microstructure. The average sliding distance per track is 0.48 ± 0.03

m of sliding distance, but the sliding distance per grains varied significantly ranging from 0.02 to

1.91 m. The differences in sliding distance can affect the rate of wear. In Figure 21, the wear

behaviors of the grains were seen to be significantly different from grain to grain. Grain 2 and 4

display an increase in wear volume as the load increases, but in grain 3, the wear loss volume can

be assumed steady as the applied normal load increases. Grain 6 shows a slight increase in the

volume loss as the normal load increases from 0.5 N to 1.0 N, but as the load increases to 1.5 N

the volume loss begins to decrease.

4.3 Main Study Part II Mg vs. MZCR

The materials involved in this study were Mg and Mg-Zn-Ca-RE alloy. The materials were fabricated into three forms: as-cast, extruded and solution heat-treated (T4). The extrusion specimens were cut along two planes to prepare test specimens: longitudinal and cross-section planes.

4.3.1   Microstructure Analysis

The grains of the MZCR (T4) are randomly distributed, as shown in Figure 22. This MZCR possesses an average grain sized of 25.08 ± 14.83 µm. The grain size is about 2 orders of magnitude smaller than the microstructure of the pure Mg from U. S. Magnesium. Surface roughness was about 80 nm after polishing.
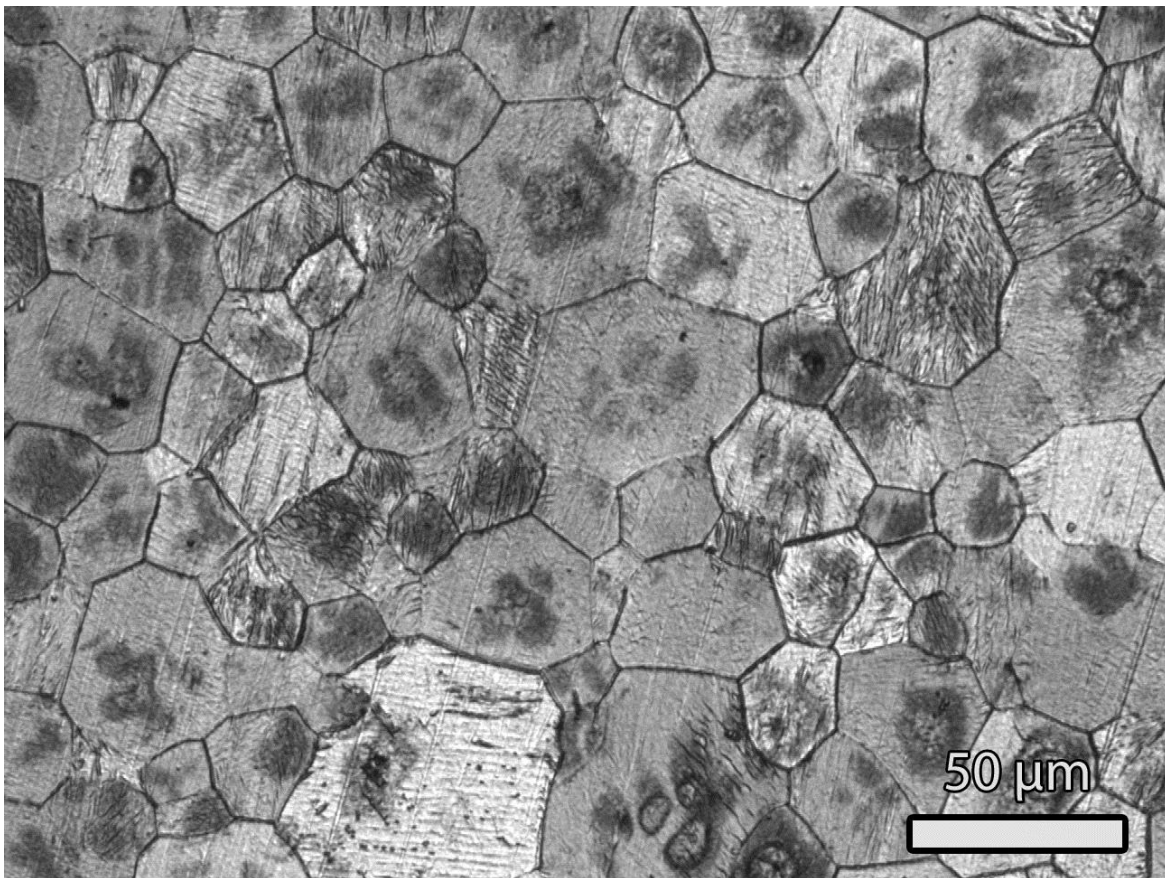

*Figure 22. M*icrostructure of MZCR-T4 (OM)

As-cast Mg has a polycrystalline structure with significantly larger grains of a few mm in size as shown in Figure 23. The average grain size of the pure Mg is 2.55 ± 1.55 mm, with average roughness of 92 nm. Twinning can be seen on the surface of the Mg grains. The extrusion process reduces grain size, as seen in Figures 24-25.
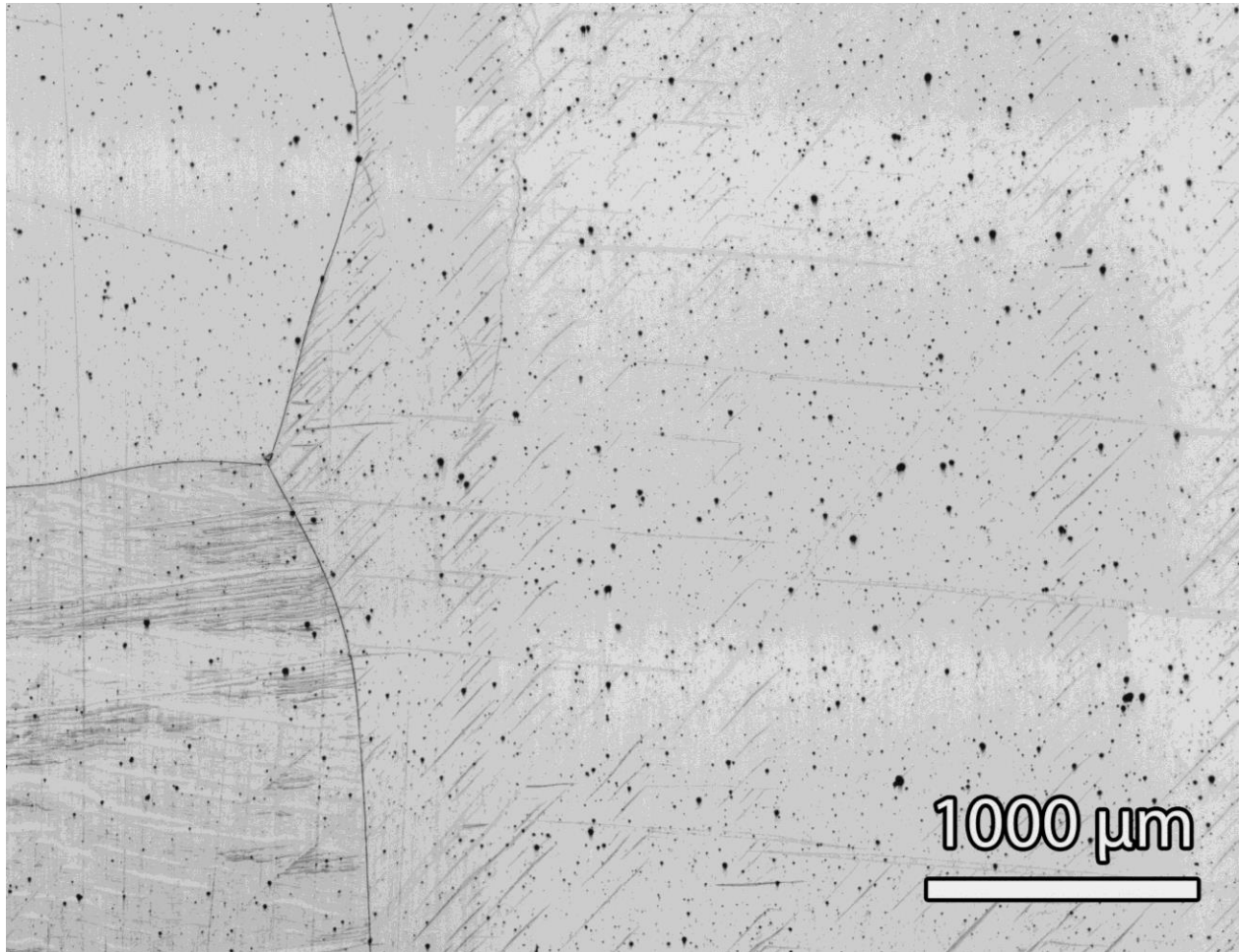
Figure 23. Microstructure of as-cast Mg from main study (OM)

The grain sizes are reduced after extrusion as shown Figure 24 and 25 of the MZCR- and Mg-ER10 longitudinal section, respectively. The surface of the longitudinal section of MZCR-ER10 has series of defects along the extrusion direction. The average grain size in this material is 2.23 ± 2.23 µm.

Figure 24. Microstructure of MZCR-ER10 longitudinal section (OM)

Figure 25. Microstructure of Mg-ER10 longitudinal section (OM)

Figure 26. Microstructure of MZCR-ER10 cross-sectional plane (OM)
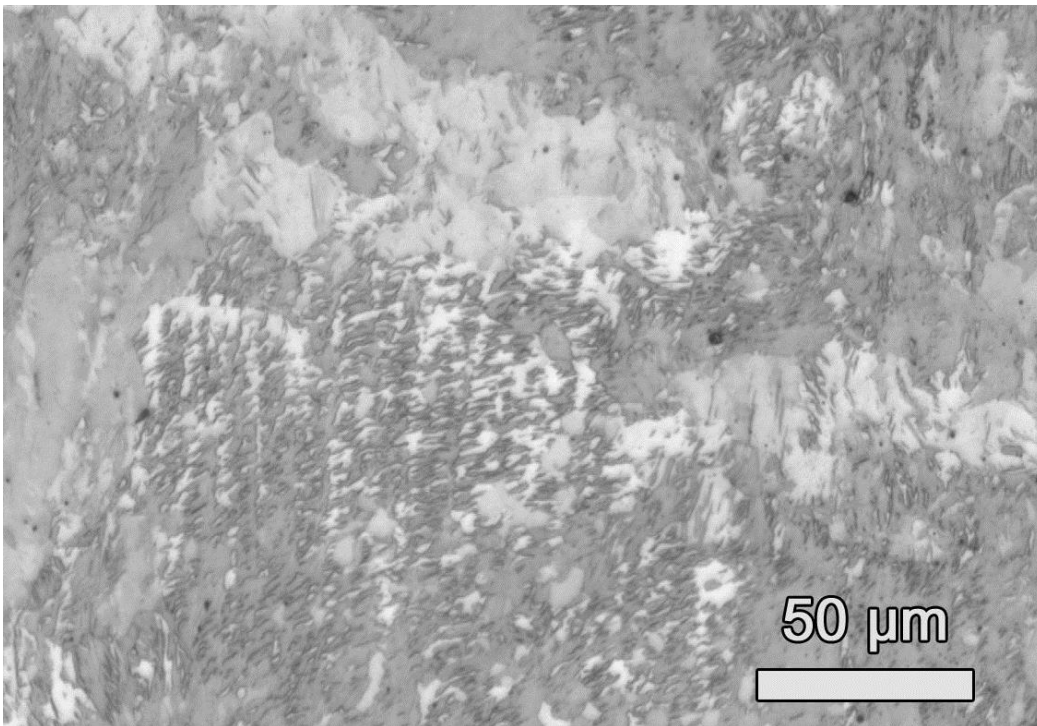
Figure 27. Microstructure Mg-ER10 cross-sectional plane (OM)

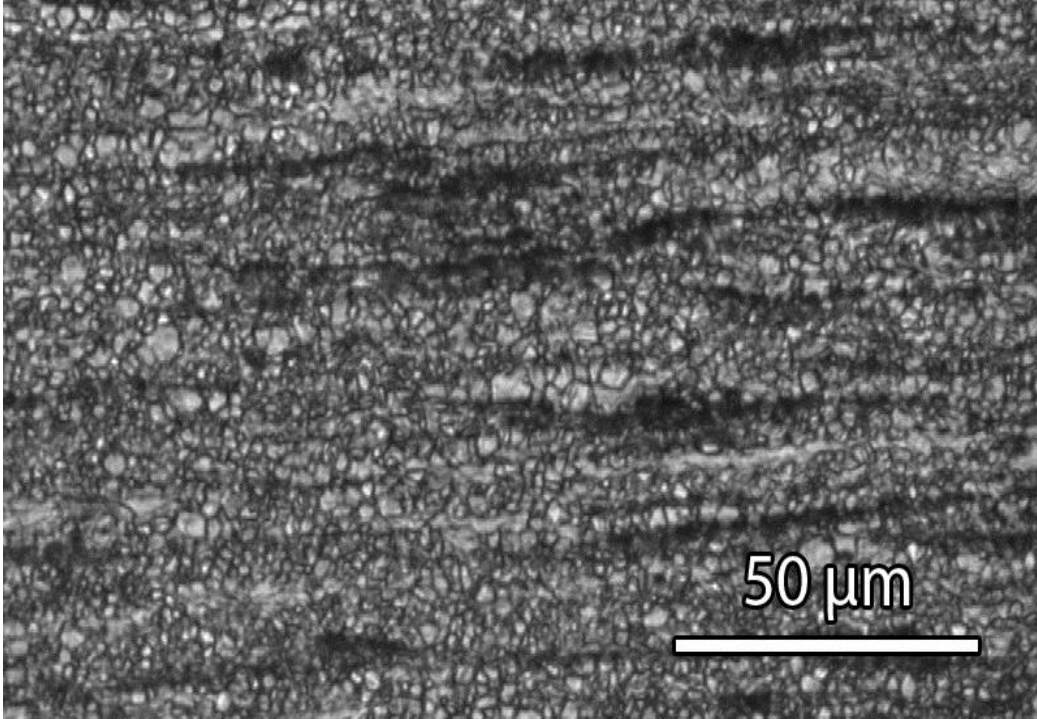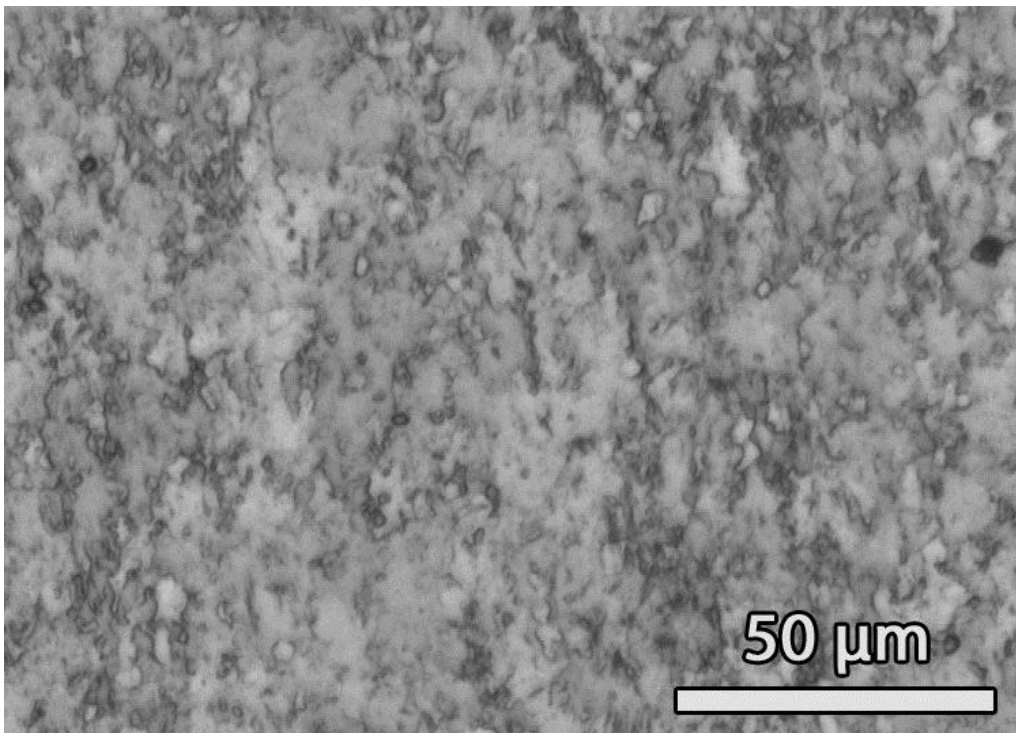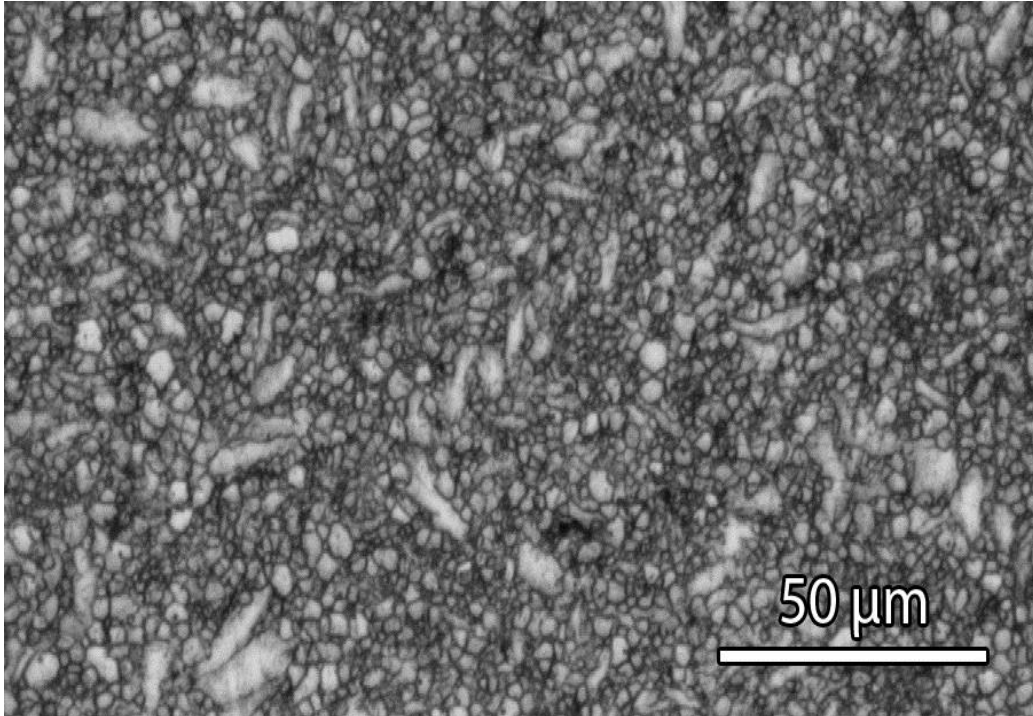The cross-section plane of MZCR-ER10 is shown in Figure 26. The cross-section has grains that are randomly distributed varying in sizes. The average grain size of the MZCR-ER10 cross-section is 3.18 ± 1.73 μm Figure 27 shows the cross-sectional plane of the Mg-ER10. The microstructure of the Mg-ER10 cross-sectional plane does not have well-defined grain boundaries.
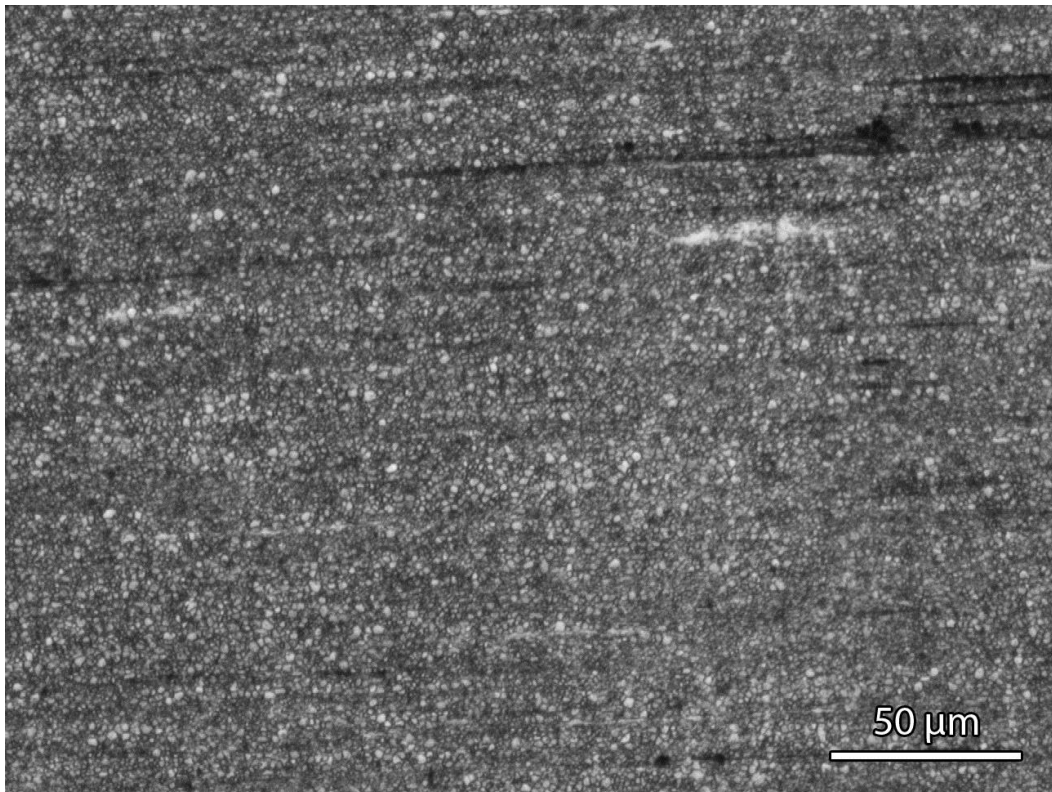
Figure 28. Microstructure MZCR-ER50 longitudinal section (OM)

The extrusion process continues to reduce the grain-size in the microstructure of both materials. The MZCR-ER50 displays fewer defects along the extrusion direction in the longitudinal plane compared to the ER10. The grains continue to reduce in size as the extrusion process continues to decreases the cross-sectional area. The average grain size of this material is 1.78 ± 0.93 μm. Figure 29 shows the microstructure of the extruded Mg-ER50 longitudinal section. The grains in this microstructure become smaller, just as in the case of the MZCR. The

grains were measurable in this specimen averaging a grain size of 3.27 ± 2.81 µm. The Mg

grains size after extrusion reduces, but is still larger than the MZCR grains.
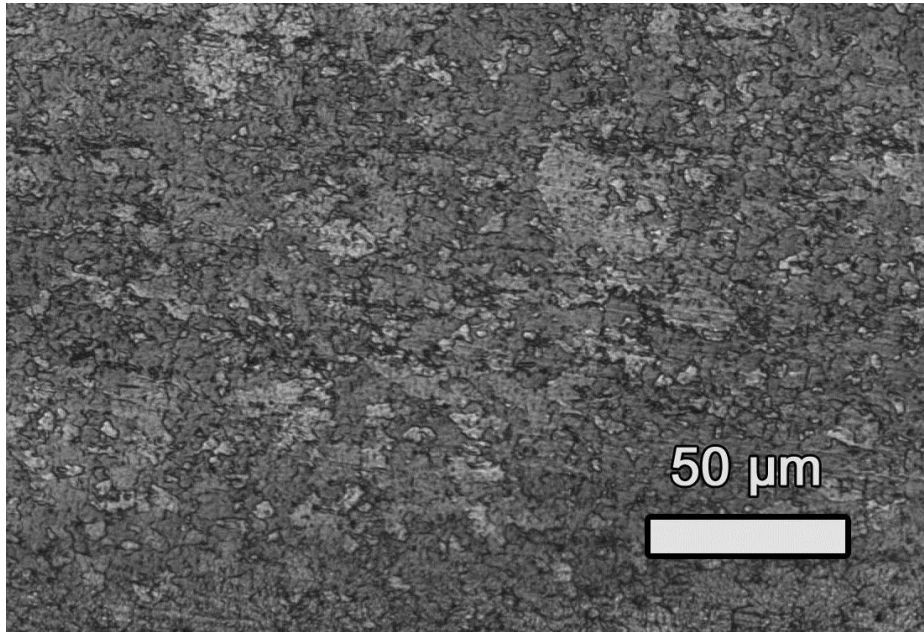
Figure 29. Microstructure of Mg-ER50 longitudinal section (OM)
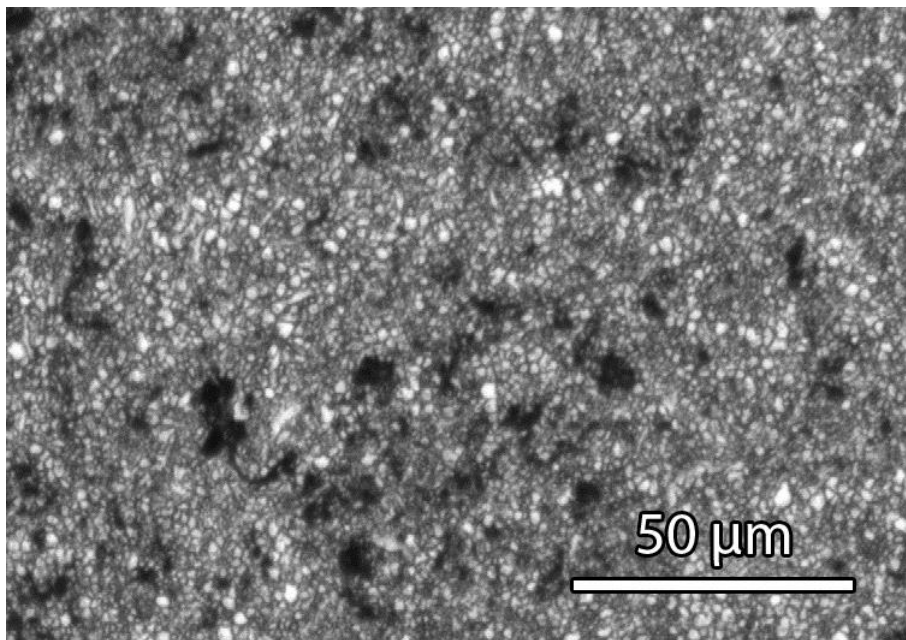
Figure 30. Microstructure of MZCR-ER50 cross-section (OM)

The microstructure of the Mg and MZCR-ER50 cross-section is shown in Figures 30 and 31. The grain size of the MZCR is 1.82 ± 0.95 μm. Defects are present on the surface of the MZCR unlike in the case of pure Mg. The cross-section of the magnesium has scratches on the surface that could have been by the polishing errors. The grain sizes of the Mg are larger than the grain of the MZCR.. For both materials, the cross-section display slightly larger grain size than the longitudinal section.
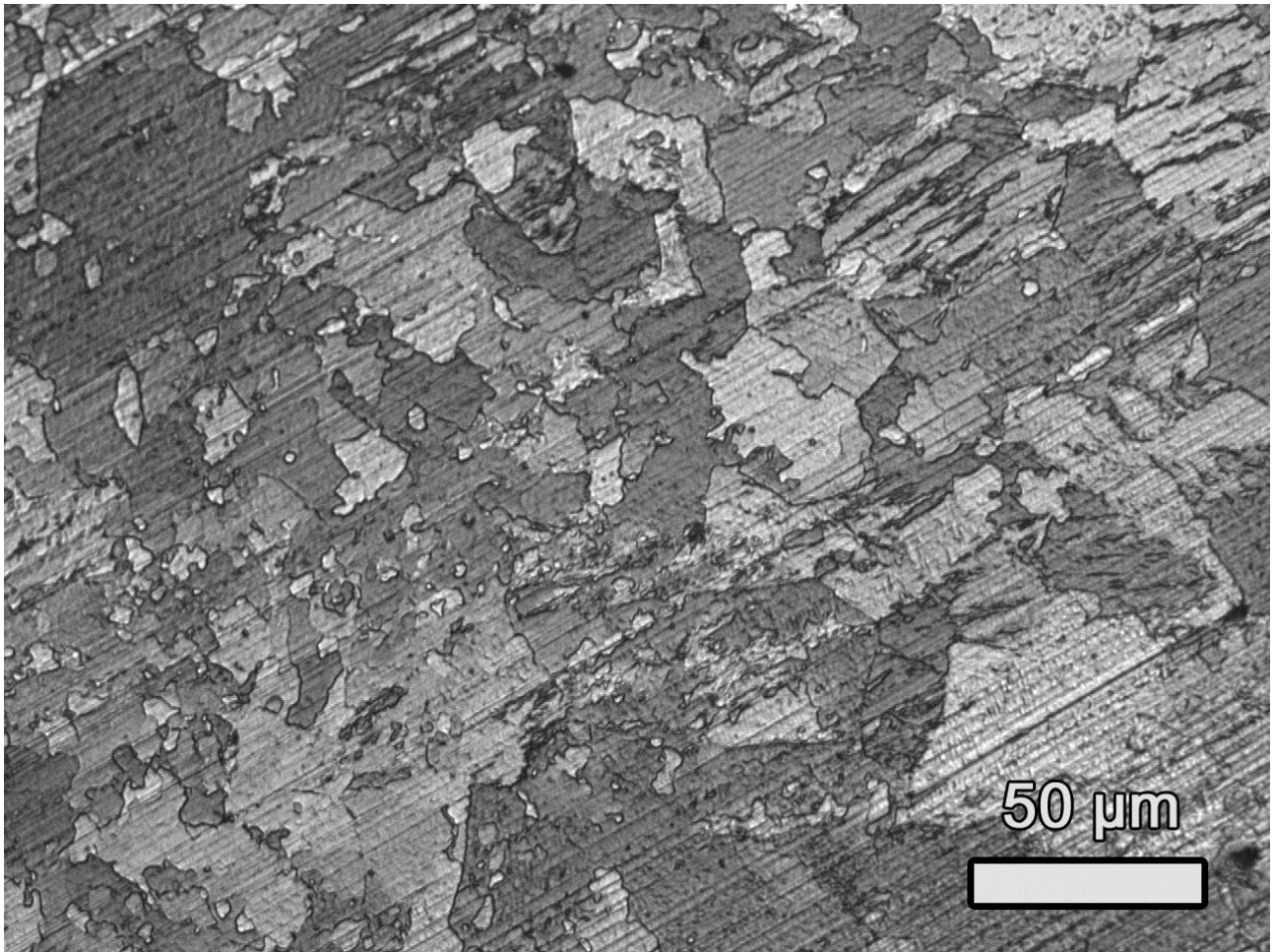
Figure 31. Microstructure - Mg-ER50 cross- section

4.3.2   Surface Morphology of Wear-Tested Specimens

Scanning electron microscopy was carried out on the specimens in the main study. The wear track morphology and wear debris of the Mg and MZCR alloys were analyzed.

4.3.2.1   *Abrasion and Adhesion Wear*

Figure 32 shows the surface morphology of the T4 heat treated alloy at 2.5 N applied normal load at 120 cycles. A large wear groove is formed on the worn surface, followed by flaking of materials and other fine particles resting on the track.

NCAT 5.0kV 8.4mm x500 SE(UL)   100um
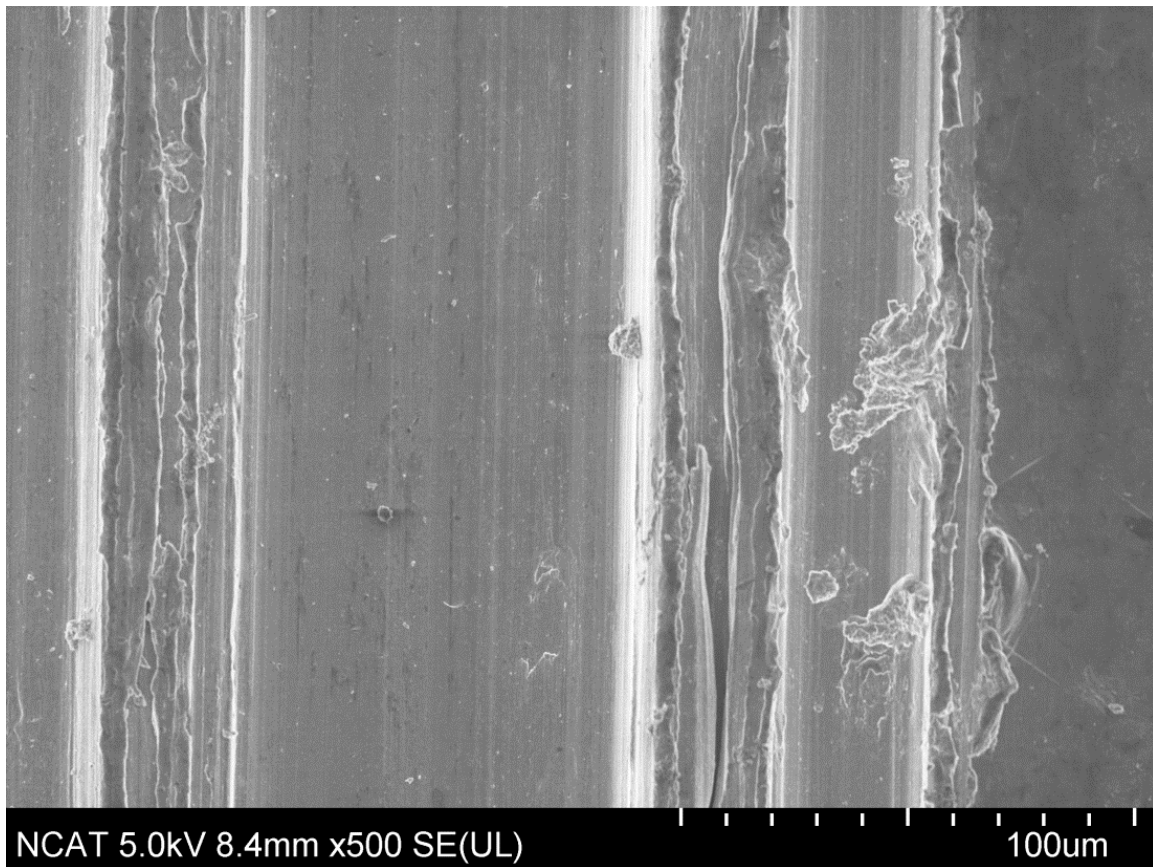
Figure 32. Wear track on T4 heat-treated MZCR (2.5 N normal load)

The generation of the groove is proof that abrasion is one of the mechanisms involved. From Figure 27, the abrasive wear mechanism is evident due to the groove in the surface. Bayer

[81, 82] defined abrasion wear as a wear mechanism associated with hard protuberances or particles that resulted in grooves, scratches, or indentations. In this case, the sapphire counterface hardness is greater than the hardness of the Mg and MZCR, resulting in ploughing of the material.
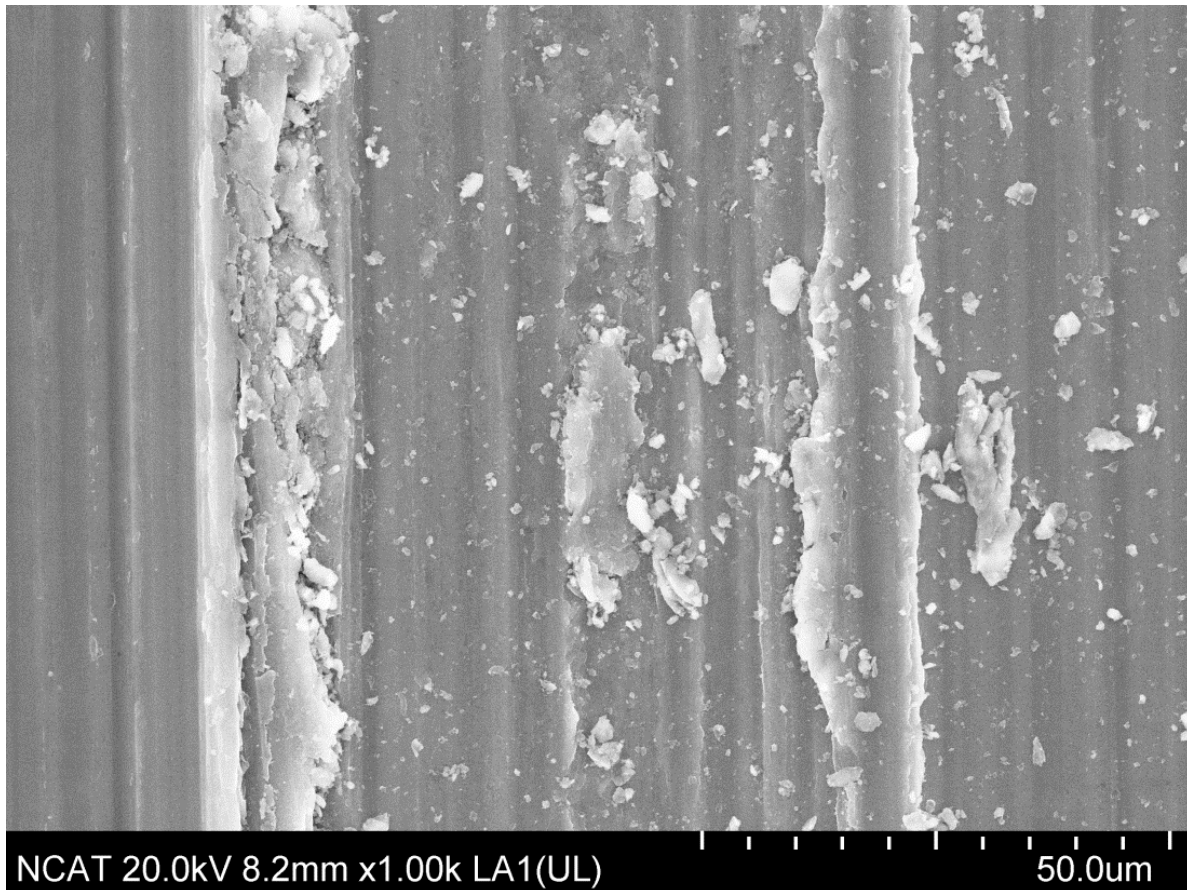
Figure 33. Wear track on Mg-ER50 cross-section (0.5 N normal load)

Figure 33 displays the surface topography of the wear track of the Mg-ER50 cross-section subjected to a normal load of 2.5 N. The abrasive wear mechanism is present on the surface of the Mg-ER50 cross-section. A series of wear grooves are present in the worn region of the surface. Figure 34 shows the wear track on the Mg-ER50 longitudinal section surface for an applied normal load of 0.5 N. A series of grooves is seen on the surface of the Mg-ER50. The

generations of wear particles that are resting on the worn surfaces indicate that three-body

abrasive wear was the mechanism involved in the creation of this wear track. The grooves are

non-uniform in size and some of the wear particles are resting around or have merged with the

wear track.
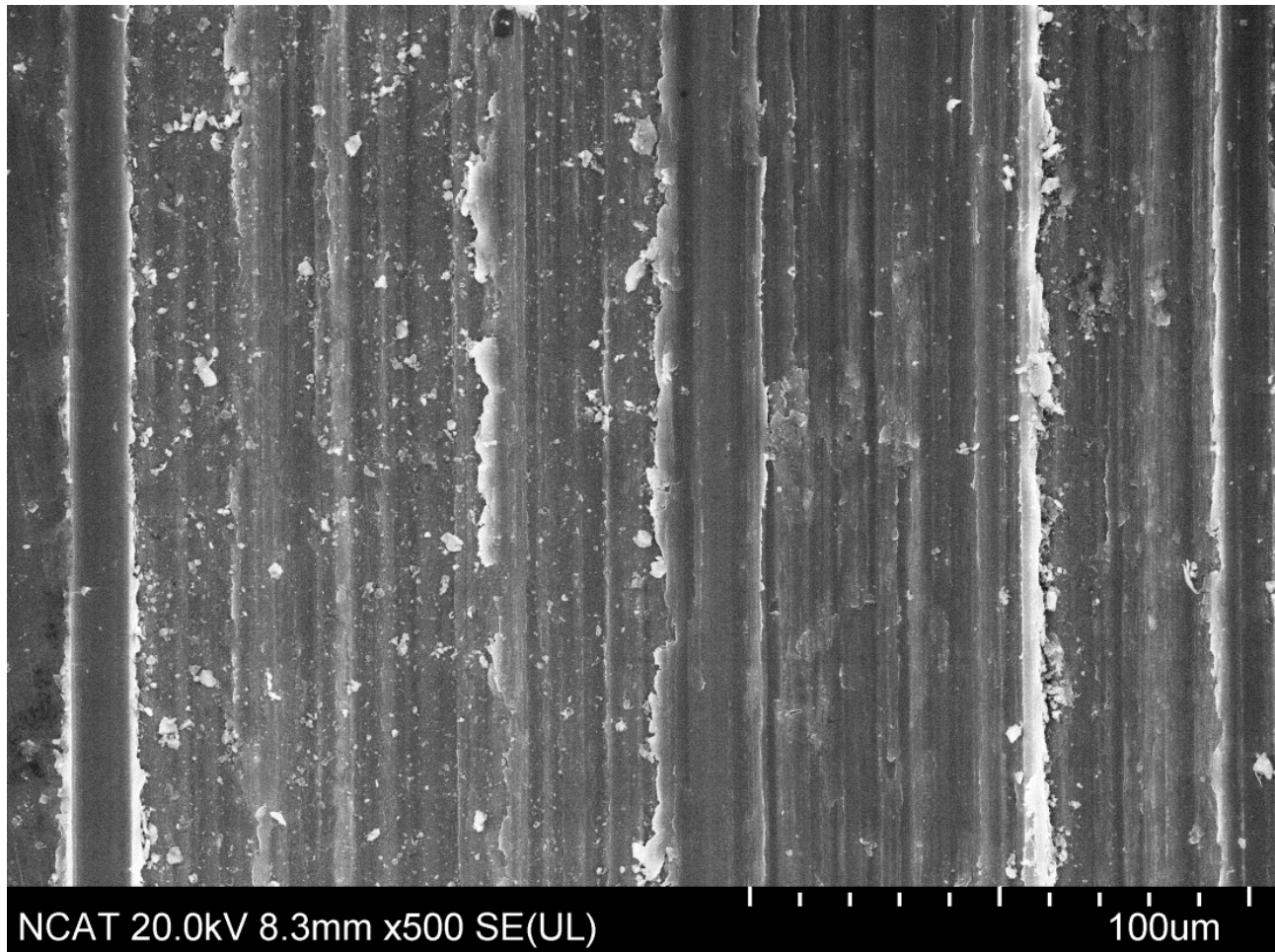
Figure 34. Wear track on Mg-ER50 longitudinal section along the transverse direction (0.5 N normal load)

Figure 35 shows the wear track on the Mg-ER50 longitudinal section along the extrusion

direction. Large wear grooves are located in the wear region, indicating abrasive wear. The

source of the abrasive wear in this study comes from the use of the sapphire counterface. The

counterface hardness is approximately 6 times and 4 times harder than the Mg and MZCR, respectively.
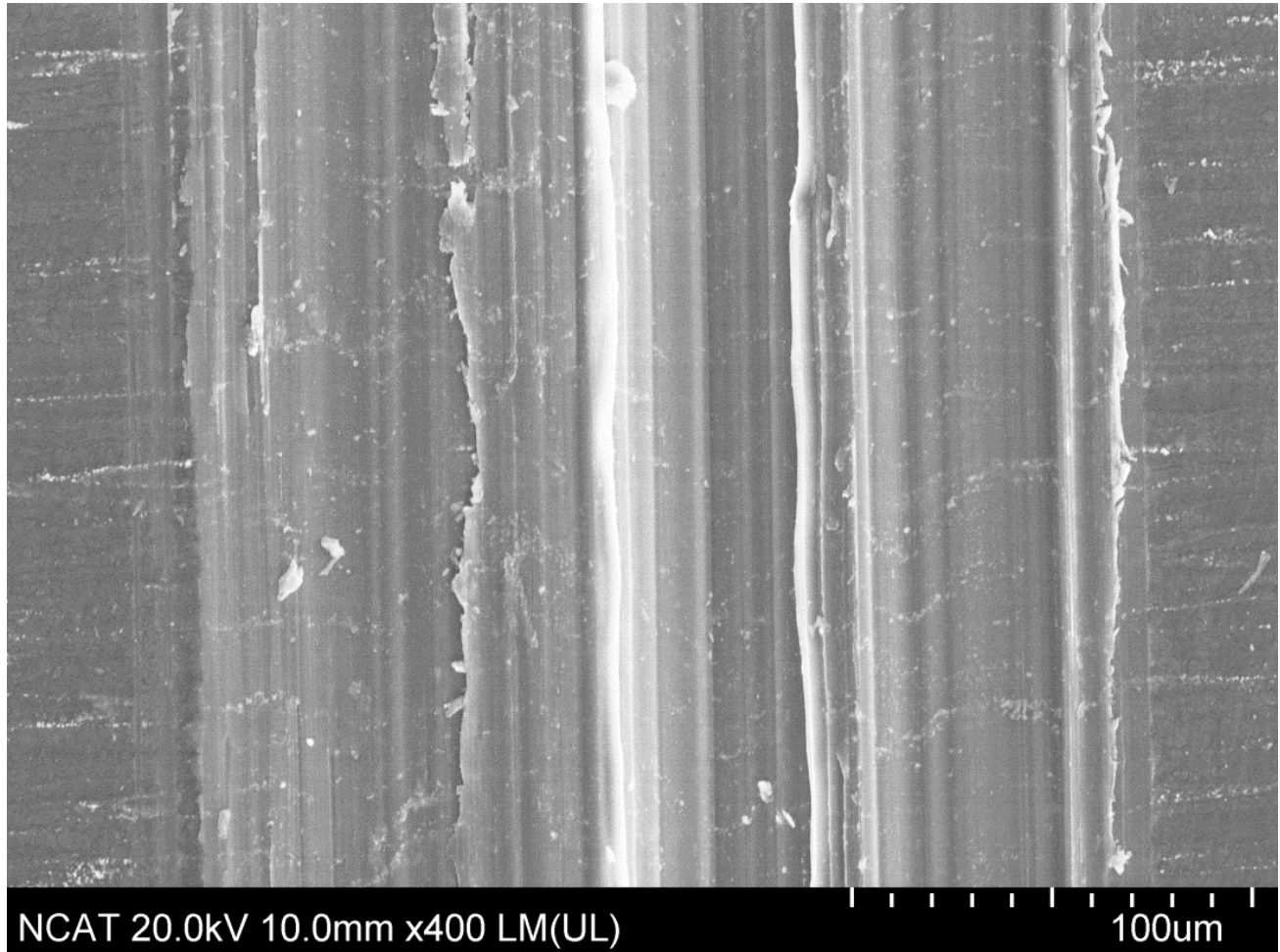
Figure 35. Wear track on Mg-ER50 longitudinal section along the extrusion direction (0.5 N normal load)

Figure 36 shows the optical micrograph of MZCR particles attached to the surface of the sapphire specimen. The MZCR adheres to the surface of the sapphire, which provides evidence of adhesive wear. Bayer [81, 82] defines adhesion wear as wear occurring when one of the contacting surface is transferred onto the other surface at localized sites. After each wear test, the sapphire counterface was observed to detect any particles adhering to it.
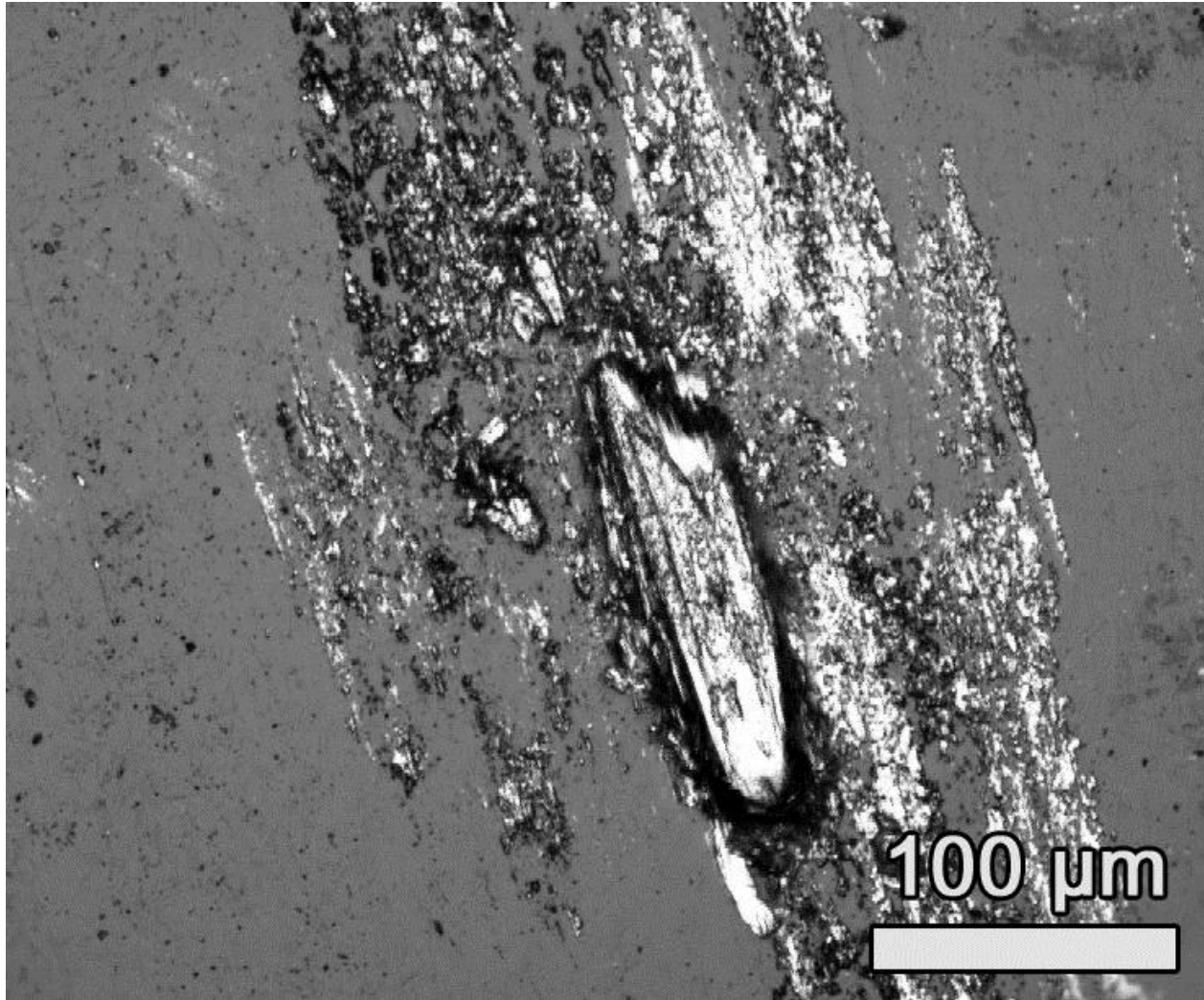
Figure 36. Sapphire counterface surface after wear test, showing adhesive wear.

It was observed that as the normal load increases, the rate of adhesive wear increases, which is shown by the amount of material transferred to the opposing counterface. The counterface was imaged before and after cleaning of the counterface. The counterface was cleaned off with compressed air and the image above shows the counterface after cleaning. The amount of material that is still present on the sapphire counter indicates that two-body and three-body abrasive wear was the active wear mechanism during the main study.

4.3.2.2 *Fatigue and Delamination Wear*

Fig. 37 is a SEM micrograph of the wear track of Mg-ER10 under applied normal load for 2.5 N at 120 cycles.

NCAT 10.0kV 8.2mm x500 SE(UL)   100um
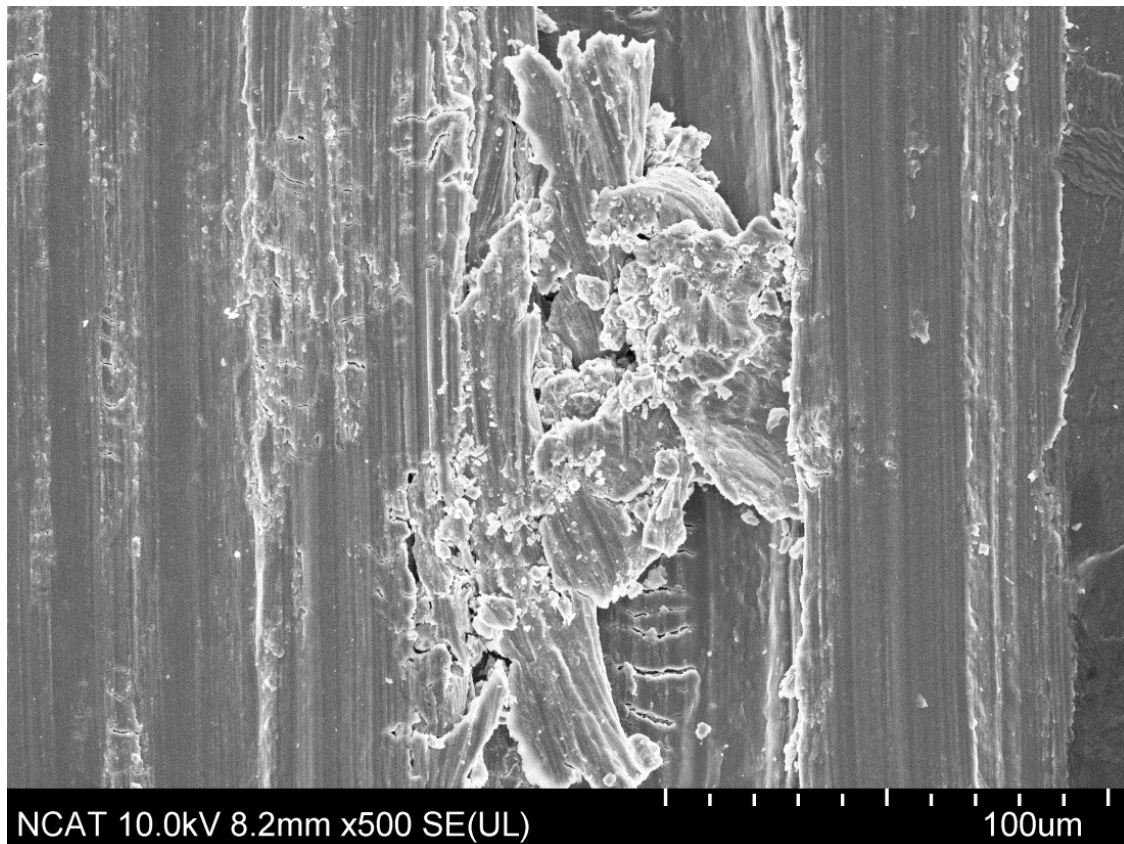
*Figure 37. W*ear track on Mg-ER10 cross-sectional (2.5 N normal load).

It is evident that there are cracks formed in the worn region. The Mg-ER10 experiences plastic deformation from the sapphire, which generates cracks on the surface. The cracks in the worn surface indicate fatigue wear. Fatigue wear is a wear mechanism under repeated sliding, rolling, or impacting where the material's surface experiences cyclic stress that initiates cracks [81-83]. The increase in applied normal load caused in plastic deformation, resulting in extensive damage to the materials.
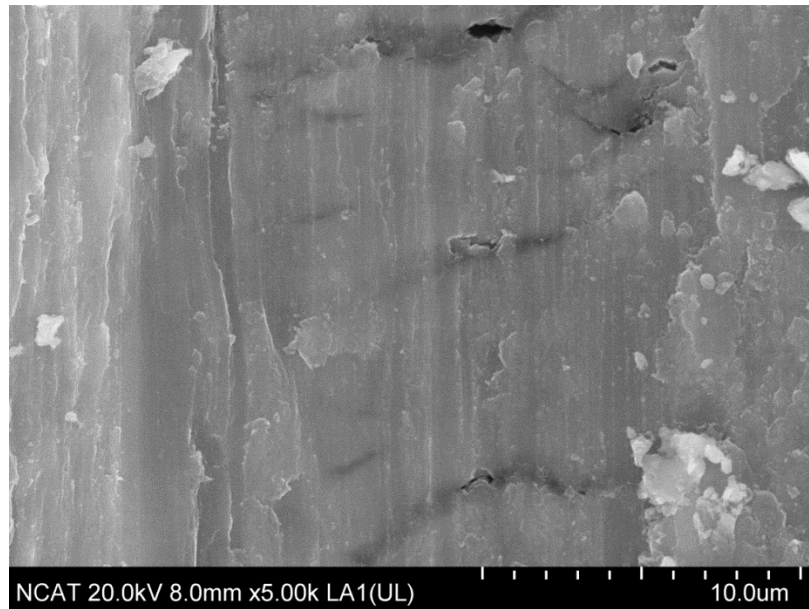
Figure 38. Wear track on Mg-ER50 cross-section (1.5 N normal load)
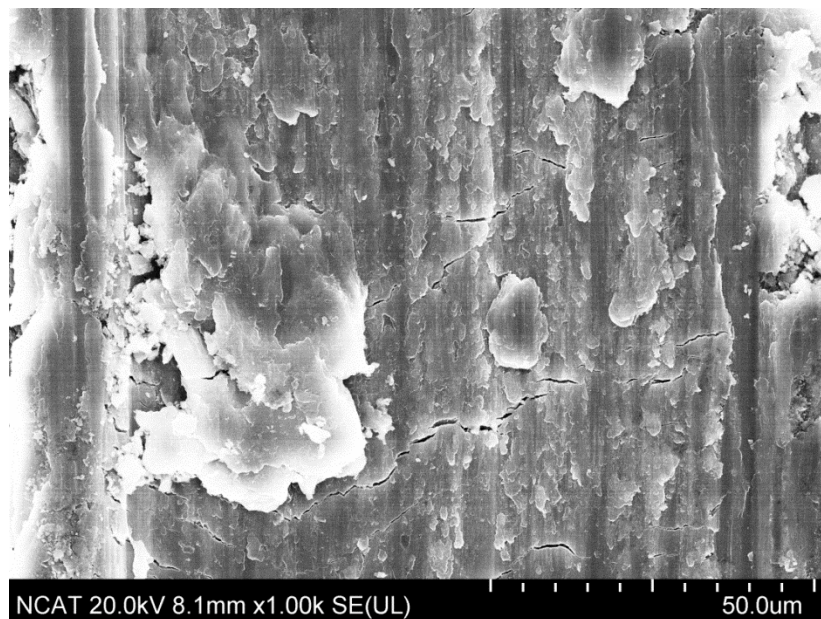
Figure 39. Wear track on Mg-ER50 cross-section (2.0 N normal load)

Figures 38 and 39 are SEM micrograph of the cracks in the subsurface and surface of the

Mg-ER50 cross-section. Fatigue wear was found in the worn region of Mg in all of the wear

testing done in the main study. Cracks were not observed on the surface of the MZCR alloy.

Figure 40 shows the wear track of MZCR-ER50 in the cross-sectional plane under applied load of 2.5 N. Material has begun detaching from the surface in thin plate-like particles.

Figure 40. Wear track on MZCR-ER50 in the cross-section (2.5 N normal load)

Delamination wear is the result of the connection of cracks to cause wear particles to detach from the specimen surface. According to [81-83], delamination occurs when plastic flow nucleates and promotes of the growth of subsurface cracks that propagate parallel to the surface, before extending out to the free surface to form platelet-like wear particles. Delamination wear and fatigue wear can occur simultaneously. Delamination wear was found frequently on the surface of both Mg and MZCR specimens.

4.3.3   Microhardness

Alloying and extrusion increase the hardness of the MZCR. Microhardness testing was conducted on Mg and MZCR in longitudinal section and cross-section. Alloying of magnesium with Ca, Zn and RE enhances the hardness properties by over 50%. Extrusion of Mg actually decreases the hardness as the extrusion ratio increases. The longitudinal section of Mg-ER10 shows higher hardness compared to the cross-section. The extrusion of the as-cast MZCR decreases the hardness value when the ratio reaches 10, but increases at ratio 50. The hardness of the MCZR-ER10 longitudinal section is greater than the cross-section plane. The hardness of the MZCR-ER50 trends completely opposite compared to MZCR-ER10. The hardness of the MZCR-ER50 cross-section is slightly harder than longitudinal section. The results show that as the extrusion ratio increases from 10 to 50, the hardness value increases, surpassing the as-cast MZCR.
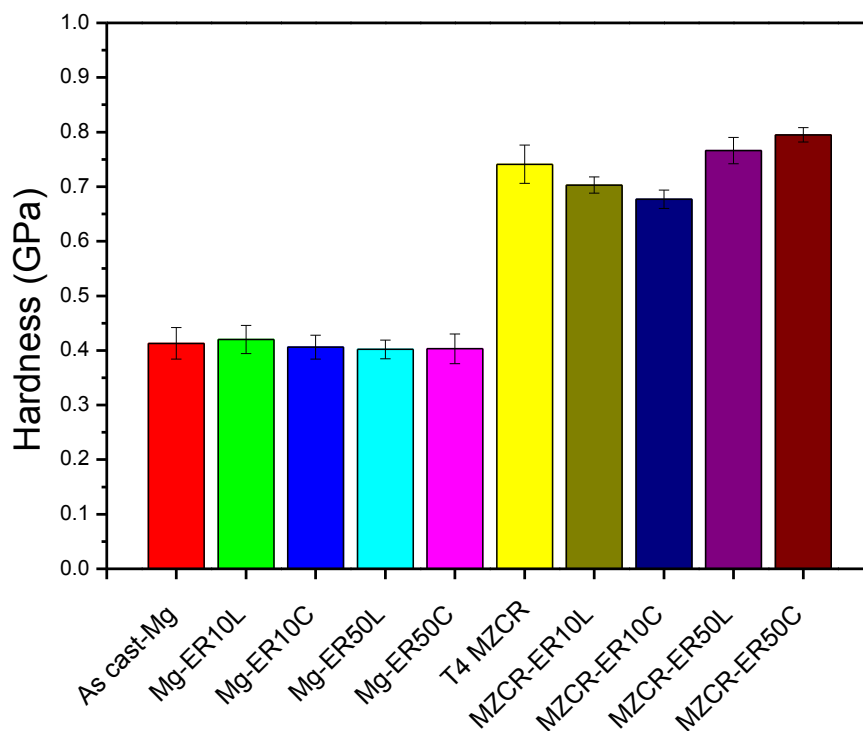
Figure 41. Hardness of Mg and MZCR specimens

4.3.4 Wear Test Analysis

In the main study, a combination of techniques was used to evaluate the wear behavior of the Mg and MZCR. Mictribometery was used to evaluate the wear and friction properties of Mg and MZCR under a sapphire counterface, and microindentation to measure the hardness. As Table 5, a total of 195 wear tests, 1950 cross-sectional measurements of wear track, and 212 indents were made.

Table 5. Main study summary

Process	Test plane	Test direction	# of wear tests	# of cross-sectional area measurements	No of Vickers indentations
Pure Mg					
As-cast	N/A	*	15	150	20
ER10	L	LD	45	450	22
		TD			
	C	*			27
ER50	L	LD	30	300	22
		TD			
	C	C			19
MZCR					
As-cast	N/A	*	15	150	22
ER10	L	LD	45	450	20
		TD			
	C	*			20
ER50	L	LD	45	450	20
		TD			
	C	C			20
Total			**195**	**1950**	**212**

* not relevant/not available.
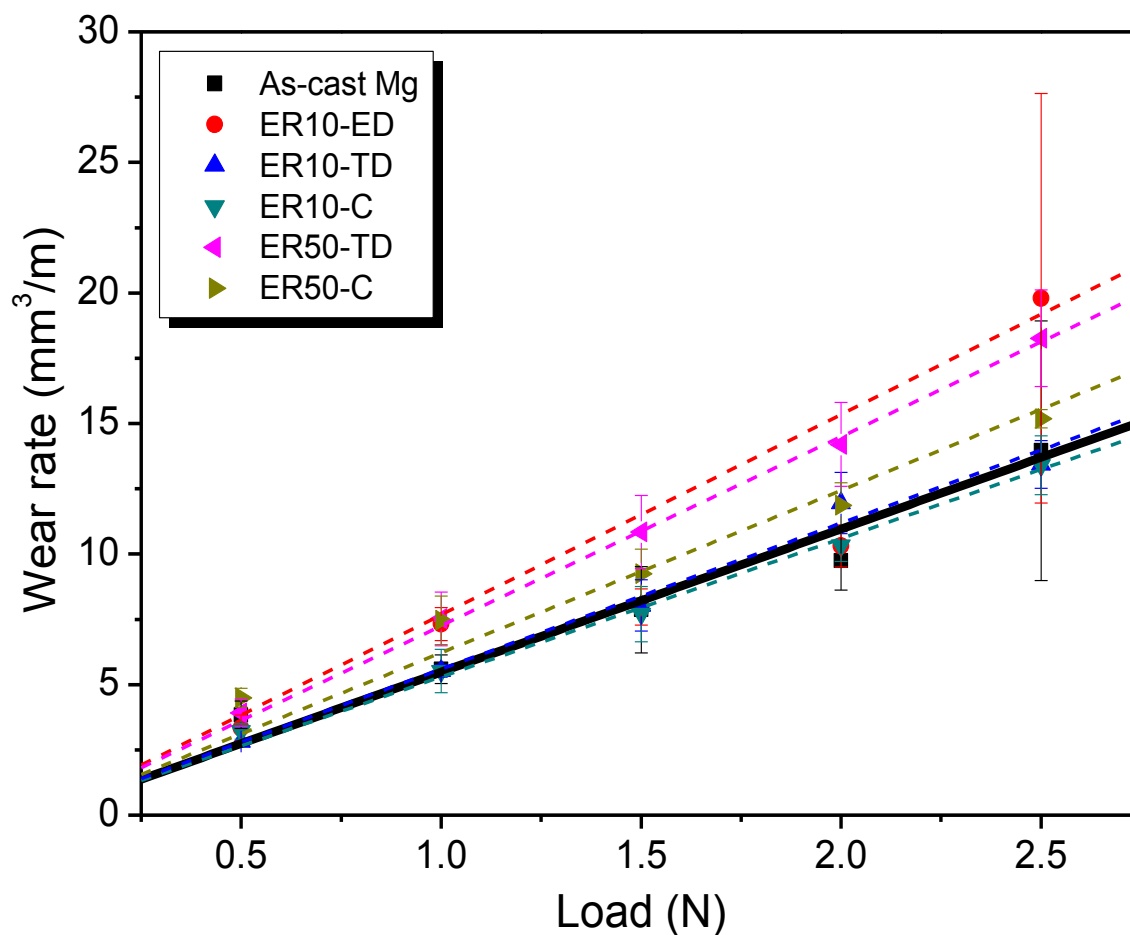
Figure 42. Effect of applied normal load on wear rate of Mg

Figures 42 and 43 show the variation in wear rate with respect to the normal load for the

Mg and MZCR, respectively. The solid black lines in both of the figures represent the wear rates

of the as-cast Mg and the MZCR, respectively. The Mg and MZCR are seen to exhibit different

and opposite behaviors in wear properties after the extrusion. The as-cast Mg has a higher wear

resistance compared to as-cast T4 heat-treated MZCR, despite their difference in hardness. The

hardness of as-cast MZCR-T4 is 1.80 times greater than that of Mg. Extrusion is found to greatly

affect wear performance. For Mg, the wear resistance decreases as the cross-sectional area of the

extruded sample decreases. The opposite occurs in the MZCR, where the wear resistance

increases after extrusion.
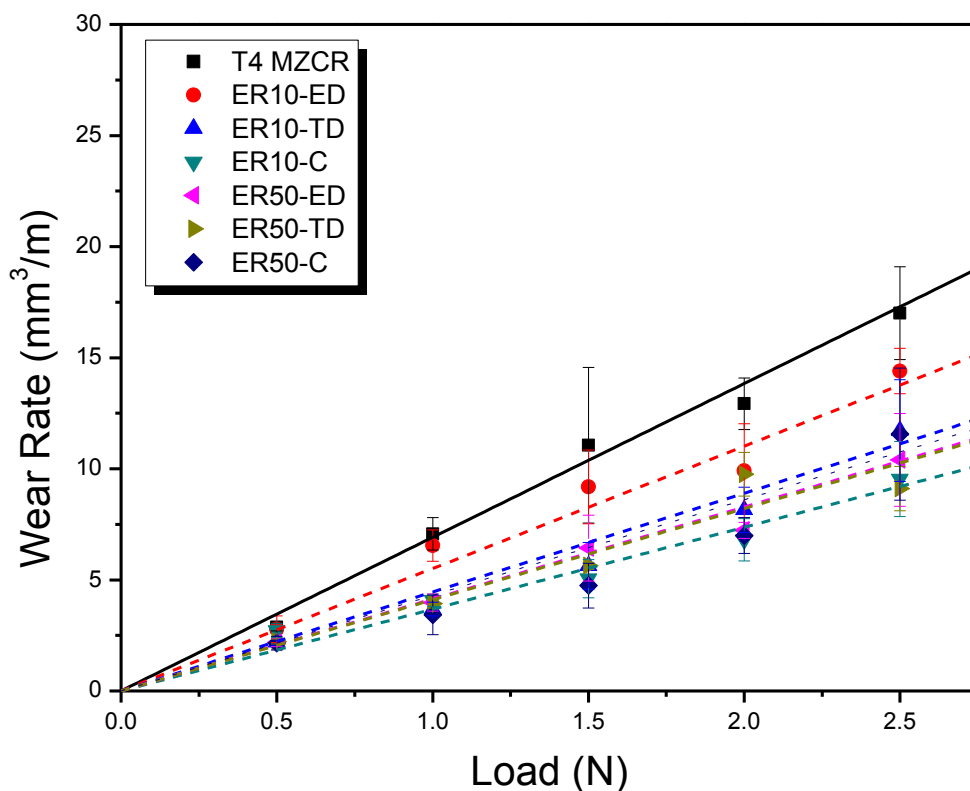
Figure 43. Effect of normal applied load on the wear of MZCR

The Mg specimen extruded to ER10 has a lower wear rate along the cross-section than as-cast Mg. According to the Figure 41, the cross-sectional plane under extrusion ratio 10 has the lowest hardness compared of all the Mg specimens. The cross-sectional plane of the Mg-ER50 display a lower wear rate compared to the longitudinal section. The Mg-ER10 in the longitudinal section displayed favorable wear resistance along the transverse direction.

Similar to the Mg-ER10, the cross-sectional plane of the MZCR-ER10 displays low wear rate and hardness compared to the rest of the MZCR specimens. The wear resistances of the MZCR-ER50 in both the longitudinal and cross-section planes are similar. The longitudinal plane of the ER10 along the extrusion direction in both the Mg and MZCR appear to have the highest wear rates. The behavior of the Mg and MZCR are reflected by the wear coefficient.

Table 6. Main study wear summary of Mg and MZCR

Material conditions	Coefficient of friction, μ ± err(0.95)	Vickers hardness (GPa) ± err(0.95)	Specific wear rate, k (mm^3/N·m) ± err(0.95)	Ratio of wear rates	Wear coefficient, K ( )
Pure Mg					
As-cast	0.367 ± 0.006	0.413 ± 0.014	5.49 ± 0.79	1.00	2.27
ER10-C	0.351 ± 0.005	0.406 ± 0.009	5.30 ± 0.39	1.04	0.215
ER10-LD	0.366 ± 0.003	0.420 ± 0.012	7.65 ± 0.43	0.72	3.21
ER10-TD	0.345 ± 0.011	0.420 ± 0.012	5.59 ± 0.24	0.98	2.35
ER50-C	0.350 ± 0.003	0.403 ± 0.013	6.22 ± 0.26	0.88	2.51
ER50-LD	*	0.402 ± 0.008	*	*	*
ER50-TD	0.309 ± 0.045	0.402 ± 0.008	7.25 ± 0.06	0.76	2.91
MZCR					
T4	0.323 ± 0.004	0.740 ± 0.013	6.92 ± 0.65	1.00	5.13
ER10-C	0.308 ± 0.004	0.677 ± 0.008	3.68 ± 0.50	1.88	2.49
ER10-LD	0.316 ± 0.006	0.703 ± 0.007	5.51 ± 0.54	1.26	3.87
ER10-TD	0.301 ± 0.004	0.703 ± 0.007	4.45 ± 0.35	1.56	3.13
ER50-C	0.293 ± 0.004	0.795 ± 0.011	4.30 ± 0.49	1.61	3.42
ER50-LD	0.292 ± 0.003	0.766 ± 0.006	4.14 ± 0.33	1.67	3.17
ER50-TD	0.296 ± 0.004	0.766 ± 0.006	4.10 ± 0.30	1.69	3.14

∗   not recorded (equipment malfunction)

The specific wear rate was extracted from the slope of the wear rate. Multiplying the specific wear rate with the hardness will provide the wear coefficient of the system. In Table 6, the wear coefficients of Mg and MZCR are significantly different. Similarly, the shift in the wear rate slope after the extrusion process climbs, indicating that extrusion is decreasing the wear resistance of Mg. The opposite effect is seen in MZCR, i.e. the extrusion process increases the wear resistance. The lowest amount of wear occurred in the specimen with the lowest hardness. According to Table 6, the coefficient of friction decreases as the extrusion ratio increases. The wear rate of the extruded Mg decreases as long as the coefficient of friction is below 0.366. The wear rate decreases in the extruded MZCR as long as the coefficient of friction is below 0.316.

CHAPTER 5

Conclusions and Recommendations for Future Work

5.1 Conclusion

The purpose of this research was to develop a technique that would aid in material selection for magnesium based alloys that will be subjected to wear in various biomedical applications. Microtribometery was used to evaluate the wear properties of magnesium alloys. Various combinations of parameters were considered in the development the wear technique. Materials were wear-tested under reciprocating motion under normal loads of 0.5, 1.0, 1.5, 2.0, and 2.5 N. Wear was characterized using optical microscopy, scanning electron microscopy, and stylus profilometry. Optical microscopy was used to analyze the surface morphology prior to wear testing. The optical images were used to measure the stroke length of the wear track that can be used to calculate the sliding distance. Scanning electron microscopy was used to identify the operational wear mechanisms. Stylus profilometry was used to measure the wear area of the worn surface.

- Pilot study: Al vs. Goodfellow–supplied Mg
  - The purpose of the wear tests was to establish a technique that would be highly accurate and repeatable. It was discovered that even after polishing the surface, the surface may still not be level with respect to the wear test strokes, which can affect the upper specimen ability to maintain uniform contact during testing. Specimen alignment was carried out in order to optimize the reciprocating contact between the upper and lower specimen.

- o Aluminum possesses a higher wear resistance compared to magnesium. The overall wear rate measurements were repeatable. When the technique was applied to another pure Mg (U.S. Magnesium,) however, the wear data showed up to 92% variation in wear data. A microstructural evaluation sparked by this anomalous result led to the conclusion that the variation of wear rates observed in the main study Mg was due to the outsized grains in that specimen. The wear behavior of the Mg varied from grain to grain because the stroke length was small relative to the grain length..

- Main study: Mg vs. MZCR

  - o The established technique from the pilot study was used on the as-cast and extruded specimen in order to evaluate the tribological properties in the main study.

  - o The extruded Mg and MZCR alloy were cut along two planes: longitudinal and cross-section. Directional wear testing was applied to the longitudinal section.

  - o Deformation processing was found to have contrasting effects on the wear resistance

    - ▪ Extrusion of Mg shown has a negative effect on its wear properties; with an increasing extrusion ratio significantly decreasing the wear resistance.

    - ▪ Extrusion of MZCR enhances the hardness and wear property, with an increase in extrusion ratio also increasing the hardness and wear resistance.

  - o The cross-sectional plane displays higher wear resistance than the longitudinal plane, despite low hardness measured on the cross-sectional plane

  - o In the longitudinal plane, wear in the transverse direction is lower compared to the extrusion direction.

  - o Fatigue wear is one of the wear mechanisms observed in Mg.

  - o Abrasive, adhesive and delamination wear were found in both Mg and MZCR.

o   High precision was achieved using the technique, with errors below 7%.

- The wear technique developed in this study is suitable for materials with grain sizes under 100 μm.

- The combination of alloying and extrusion is beneficial for improvement of wear resistance.

5.2 Future Work

Future wors can focus on expansion of the wear techniques under various parameters and configurations, not addressed in this study, to more comprehensively evaluate materials. Expansion of the wear technique can include biodegradable alloys subjected to wear in corrosive environments more like the real environments in various biomedical applications. Establishment of a tribocorrosion testing technique is needed to analyze the material behavior under stress in corrosive environments so as to gain insight to support performance-driven alloys and processes. Such tribocorrosion study would include wear testing in corrosive environments mimicking *in vivo* conditions to study the effect of alloying elements, texture, and surface modifications.

References

1. Initiative, T.U.S.B.a.J., *Burden of Musculoskeletal Disease Overview.* American Academy of Orthopaedic Surgeions, 2011.

2. Surgeons, A.A.o.O., *Children and Musculoskeletal Health.* Americal Association of Orthopaedic Surgeons 2011.

3. Burden, B.a.J., *Musculoskeletal Injuries.* The Burden of Musculoskeletal Diseases in the United States, 2011.

4. Kingsley, M. *Report: U.S. Demand for Implantable Medical Devices to Reach $52B in 2015*. Implantable Devices, 2012.

5. Mihalko, W.M., *Preface-Local and Systemic Effects of Wear Particles from Orthopedic Devices.* Journal of Long-Term Effects of Medical Implants 2014. **24**(1): p. 2.

6. Administration, U.S.F.a.D. *Stryker Spine-OASYS Midline Occiput Plate*. 2013; Available from: http://www.fda.gov/MedicalDevices/Safety/ListofRecalls/ucm366713.htm.

7. Niinomi, M., M. Nakai, and J. Hieda, *Development of new metallic alloys for biomedical applications.* Acta Biomater, 2012. **8**(11): p. 3888-903.

8. Pietrzak, W.S., *Principles of Devlopment and Use of Absorbable Internal Fixation.* TIssue Engineering 2000. **6**(4): p. 425-433.

9. Staiger, M.P., et al., *Magnesium and its alloys as orthopedic biomaterials: a review.* Biomaterials, 2006. **27**(9): p. 1728-34.

10. Castellani, C., et al., *Bone-implant interface strength and osseointegration: Biodegradable magnesium alloy versus standard titanium control.* Acta Biomater, 2011. **7**(1): p. 432-40.

11. Aung, N.N., W. Zhou, and L.E.N. Lim, *Wear behaviour of AZ91D alloy at low sliding speeds.* Wear, 2008. **265**(5-6): p. 780-786.

12. Hu, M.-l., et al., *Dry sliding wear behavior of cast Mg–11Y–5Gd–2Zn magnesium alloy.* Transactions of Nonferrous Metals Society of China, 2012. **22**(8): p. 1918-1923.

13. Habibnejad-Korayem, M., et al., *Tribological behavior of pure Mg and AZ31 magnesium alloy strengthened by Al2O3 nano-particles.* Wear, 2010. **268**(3-4): p. 405-412.

14. selvan, S.A. and S. Ramanathan, *Dry sliding wear behavior of hot extruded ZE41A magnesium alloy.* Materials Science and Engineering: A, 2010. **527**(7-8): p. 1815-1820.

15. López, A.J., et al., *Dry sliding wear behaviour of ZE41A magnesium alloy.* Wear, 2011. **271**(11-12): p. 2836-2844.

16. Anbu selvan, S. and S. Ramanathan, *A comparative study of the wear behavior of as-cast and hot extruded ZE41A magnesium alloy.* Journal of Alloys and Compounds, 2010. **502**(2): p. 495-502.

17. El-Morsy, A.-W., *Dry sliding wear behavior of hot deformed magnesium AZ61 alloy as influenced by the sliding conditions.* Materials Science and Engineering: A, 2008. **473**(1-2): p. 330-335.

18. An, J., et al., *Dry sliding wear behavior of magnesium alloys.* Wear, 2008. **265**(1-2): p. 97-104.

19. Wang, W., Y. Ouyang, and C.K. Poh, *Orthopaedic implant technology: biomaterials from past to future.* Ann Acad Med Singapore, 2011. **40**(5): p. 237-44.

20. Ratner, B.D. and S.J. Bryant, *BIOMATERIALS: Where We Have Been and Where We are Going.* Annual Review of Biomedical Engineering, 2004. **6**(1): p. 41-75.

21. Williams, D.F., *On the nature of biomaterials.* Biomaterials, 2009. **30**(30): p. 5897-909.

22.   Group, F., *Orthopedic Implants: US Industry Forecasts for 2012 and 2017*. 2008: Industry market Research for Business leaders, strategist, decision makers.

23.   Ratner, B.D., et al., *Biomaterials Science: An Evolving , Multidisciplinary Endeavor.* 2013: p. XXXIX.

24.   Hench, L.L. and I. Thompson, *Twenty-first century challenges for biomaterials.* J R Soc Interface, 2010. **7 Suppl 4**(Suppl 4): p. S379-91.

25.   Navarro, M., et al., *Biomaterials in orthopaedics.* J R Soc Interface, 2008. **5**(27): p. 1137-58.

26.   Hench, L.L., *Bioceramics - from Concept to Clinic.* Journal of the American Ceramic Society, 1991. **74**(7): p. 1487-1510.

27.   Ratner, B.D., *Biomaterials Science: An Introduction to Materials in Medicine*. 2004: Elsevier Academic Press.

28.   Yetkin, H., et al., *Biodegradable implants in orthopaedics and traumatology.* Turkish Journal of Medical Sciences, 2000. **30**(3): p. 297-301.

29.   Hench, L.L. and J.R. Jones, *Biomaterials, Artificial Organs and Tissue Engineering*. Woodhead Publishing.

30.   Yaszemski, M.J., *Biomaterials in Orthopedics*. 2004: M. Dekker.

31.   Best, S.M., et al., *Bioceramics: Past, present and for the future.* Journal of the European Ceramic Society, 2008. **28**(7): p. 1319-1327.

32.   Davis, J.R., *Handbook of Materials for Medical Devices*. 2003, ASM International.

33.   Binyamin, G., B.M. Shafi, and C.M. Mery, *Biomaterials: a primer for surgeons.* Semin Pediatr Surg, 2006. **15**(4): p. 276-83.

34. Muller, R., et al., *Surface engineering of stainless steel materials by covalent collagen immobilization to improve implant biocompatibility.* Biomaterials, 2005. **26**(34): p. 6962-72.

35. *Recent advances in biomaterials.* Yonsei Medical 1998. **39**(2): p. 87-96.

36. Frosch, K.-H. and K.M. Stürmer, *Metallic Biomaterials in Skeletal Repair.* European Journal of Trauma, 2006. **32**(2): p. 149-159.

37. NIINOMI, M., *Recent Metallic Materials for Biomedical Application.* Metallurgical and Materials Transactions a-Physical Metallurgy and Materials Science, 2001. **33A**: p. 477-486.

38. Seal, C.K., K. Vince, and M.A. Hodgson, *Biodegradable surgical implants based on magnesium alloys – A review of current research.* IOP Conference Series: Materials Science and Engineering, 2009. **4**: p. 012011.

39. Denkena, B. and A. Lucas, *Biocompatible Magnesium Alloys as Absorbable Implant Materials – Adjusted Surface and Subsurface Properties by Machining Processes.* CIRP Annals - Manufacturing Technology, 2007. **56**(1): p. 113-116.

40. Waizy, H., et al., *Biodegradable magnesium implants for orthopedic applications.* Journal of Materials Science, 2012. **48**(1): p. 39-50.

41. Xin, Y., et al., *Influence of aggressive ions on the degradation behavior of biomedical magnesium alloy in physiological environment.* Acta Biomaterialia, 2008. **4**(6): p. 2008-15.

42. Kraus, T., et al., *Magnesium alloys for temporary implants in osteosynthesis: in vivo studies of their degradation and interaction with bone.* Acta Biomater, 2012. **8**(3): p. 1230-8.

43. Li, N. and Y. Zheng, *Novel Magnesium Alloys Developed for Biomedical Application: A Review.* Journal of Materials Science & Technology, 2013. **29**(6): p. 489-502.

44. Zhang, B.P., et al., *Improved blood compatibility of Mg-1.0Zn-1.0Ca alloy by micro-arc oxidation.* J Biomed Mater Res A, 2011. **99**(2): p. 166-72.

45. Song, G., *Control of biodegradation of biocompatable magnesium alloys.* Corrosion Science, 2007. **49**(4): p. 1696-1701.

46. Zhang, P.B., Y. Wang, and L. Geng, *Research on Mg-Zn-Ca Alloy as Degradable Biomaterial.*

47. Janin Reifenrath, Dirk Bormann, and A. Meyer-Lindenberg, *Magnesium Alloys as Promising Degradable Implant Materials in Orthopaedic Research.* Magnesium Alloys - Corrosion and Surface Treatments, 2011.

48. Gu, X.-N. and Y.-F. Zheng, *A review on magnesium alloys as biodegradable materials.* Frontiers of Materials Science in China, 2010. **4**(2): p. 111-115.

49. Shi, P., et al., *Improvement of corrosion resistance of pure magnesium in Hanks' solution by microarc oxidation with sol–gel TiO2 sealing.* Journal of Alloys and Compounds, 2009. **469**(1–2): p. 286-292.

50. Witte, F., et al., *Degradable biomaterials based on magnesium corrosion.* Current Opinion in Solid State & Materials Science, 2008. **12**(5-6): p. 63-72.

51. Kirkland, N.T., et al., *A survey of bio-corrosion rates of magnesium alloys.* Corrosion Science, 2010. **52**(2): p. 287-291.

52. Mantripragada, V.P., et al., *An overview of recent advances in designing orthopedic and craniofacial implants.* J Biomed Mater Res A, 2013. **101**(11): p. 3349-64.

53. Disegi, J.A. and L. Eschback, *Stainless steel in bone surgery.* Injury, 2000. **31**(d): p. S-D2-1-S-D2-6.

54. Ganesh, V.K., K. Ramakrishna, and D.N. Ghista, *Biomechanics of bone-fracture fixation by stiffness-graded plates in comparison with stainless-steel plates.* Biomed Eng Online, 2005. **4**: p. 46.

55. Wang, K., *The use of titanium for medical applications in the USA.* Materials Science & Engineering A, 1996. **A**(213): p. 134-137.

56. Geetha, M., et al., *Ti based biomaterials, the ultimate choice for orthopaedic implants – A review.* Progress in Materials Science, 2009. **54**(3): p. 397-425.

57. Niinomi, M., *Recent research and development in titanium alloys for biomedical applications and healthcare goods.* Science and Technology of Advanced Materials, 2003. **4**(5): p. 445-454.

58. Mitsuo, N., *Mechanical properties of biomedical titanium alloys.* Materials Science & Engineering A, 1998(243): p. 231-236.

59. Rack, H.J. and J.I. Qazi, *Titanium alloys for biomedical applications.* Materials Science and Engineering: C, 2006. **26**(8): p. 1269-1277.

60. Niinomi, M., *Metallic biomaterials.* J Artif Organs, 2008. **11**(3): p. 105-10.

61. Elijas, C.N., et al., *Biomedical Applications of Titanium and its Alloys.* Biological Materials Sciences, 2008: p. 46-49.

62. Banerjee, R., S. Nag, and H.L. Fraser, *A novel combinatorial approach to the development of beta titanium alloys for orthopaedic implants.* Materials Science and Engineering: C, 2005. **25**(3): p. 282-289.

63.   Silva, H.M., S.G. Schneider, and C.M. Neto, *Study of nontoxic aluminum and vanadium-free titanium alloys for biomedical applications.* Materials Science and Engineering: C, 2004. **24**(5): p. 679-682.

64.   Witte, F., *The history of biodegradable magnesium implants: a review.* Acta Biomaterialia, 2010. **6**(5): p. 1680-92.

65.   Wu, G., et al., *Improving wear resistance and corrosion resistance of AZ31 magnesium alloy by DLC/AlN/Al coating.* Surface and Coatings Technology, 2010. **205**(7): p. 2067-2073.

66.   F. Živić , et al., *The potential of Magnesium Alloys as Bioabsorbable /Biodegradable Implants for Biomedical Applications.* Tribology in Industry, 2014. **36**(1): p. 67-73.

67.   Wang, M., *Developing bioactive composite materials for tissue replacement.* Biomaterials, 2003. **24**(13): p. 2133-2151.

68.   Landolt, D., S. Mischler, and M. Stemp, *Electrochemcial methods in tribocorrosion: a critical appraisal.* Elactrochimica Acta 2001. **46**: p. 3929.

69.   Bhushan, B., *Tribology in Practice Series : Principles and Applications to Tribology (2nd Edition).* Wiley.

70.   Content, W.C., *Petroleum Technology.* 2007. **1-2**.

71.   Assenova, E., et al., *Green Tribology and Quality of Life.* International Journal of Advanced Quality 2012. **40**(2).

72.   Mathew, M.T., et al., *Significance of Tribocorrosion in Biomedical Applications: Overview and Current Status.* Advances in Tribology, 2009. **2009**: p. 1-12.

73.   Teoh, S., *Fatigue of biomaterials a review.* International Journal of Fatigue, 2000. **22**: p. 825-837.

74. Milne, I., R.O. Ritchie, and B. Karihaloo, *Comprehensive Structural Integrity, Volumes 1-10*. Elsevier.

75. Kato, K., *Classification of wear mechanisms/models.* Proceedings of the Institution of Mechanical Engineers, Part J: Journal of Engineering Tribology, 2002. **216**(6): p. 349-355.

76. Stachowiak, G.W. and A.W. Batchelor, *Engineering Tribology (4th Edition)*. Elsevier.

77. Archard, J.F. and H. Hirst, *The Wear of Metals under Unlubricated Conditions.* Proceeding of Royal Society of London. Series A, Mathematical and Physical Sciences, 1956. **236**(1206): p. 397-410.

78. Glaeser, W.A., *Friction and Wear.* IEEE Transactions on Parts, Hybrids, and Packaging, 1971. **PHP-7**(2): p. 99-105.

79. Pruitt, L.A. and A.M. Chakravartula, *Mechanics of Biomaterials - Fundamental Principles for Implant Design*. Cambridge University Press.

80. Koji, K., *Abrasive wear of metals.* Tribology International, 1997. **30**(5): p. 333-338.

81. Bayer, R.G., *Engineering design for wear*. Vol. 176. 2004, New York: Marcel Dekker.

82. Bayer, R.G., *Mechanical Wear Prediction and Prevention*. 1994.

83. Mate, M.C., *Tribology on the small scale : a bottom up approach to friction, lubrication, and wea.* 2008: p. 333.

84. Pfeifer, M., *Materials Enabled Designs - The Materials Engineering Perspective to Product Design and Manufacturing*. Elsevier.

85. Budinski, K.G., *Guide to Friction, Wear, and Erosion Testing: (MNL 56)*. ASTM International.

86.   Ceram, G.B.o., *Tribology of orthopedic implants.* Med-Tech Innovation Orthopedics, 2013: p. 20-24.

87.   Designation, A.I., *E384-11: Standard Test Method for Knoop and Vicker Hardness of Materials*. 2012.

88.   Cooperation, W., *RST Plus Technical Reference Manual* 1995.

89.   Leach, R.K., *Fundamental Principles of Engineering Nanometrology*. Elsevier.

90.   International, A., *Standard Test Method for Linearly Reciprocating Ball-on-Flat Sliding Wear*. 2010.